

## Enhanced light emission performance of mixed cation perovskite films – the effect of solution stoichiometry on crystallization

Fangzhou Liu,<sup>1</sup> Xinshun Qin,<sup>1</sup> Bing Han,<sup>2\*</sup> Christopher C. S. Chan,<sup>3</sup> Chao Ma,<sup>3</sup> Tik Lun Leung,<sup>1</sup> Wei Chen,<sup>1</sup> Yanling He,<sup>1,4</sup> Ivor Lončarić,<sup>5</sup> Luca Grisanti,<sup>5</sup> Juraj Ovčar,<sup>5</sup> Željko Skoko,<sup>6</sup> Yingli Shi,<sup>1</sup> Francis Chi Chung Ling,<sup>1</sup> Md Rashedul Huque,<sup>7</sup> Juan Antonio Zapien,<sup>7</sup> Shixun Wang,<sup>7</sup> Chun-Jen Su,<sup>8</sup> U-Ser Jeng,<sup>8,9</sup> Kam Sing Wong,<sup>3</sup> Alan Man Ching Ng,<sup>4</sup> Jasminka Popović,<sup>5\*</sup> and Aleksandra B. Djurišić,<sup>1\*</sup>

<sup>1</sup>Department of Physics, The University of Hong Kong, Pokfulam Road, Hong Kong.

<sup>2</sup>Department of Materials Science and Engineering, Southern University of Science and Technology, No. 1088, Xueyuan Road, Shenzhen, Guangdong, China

<sup>3</sup>Department of Physics, The Hong Kong University of Science and Technology, Clearwater Bay, Hong Kong

<sup>4</sup>Department of Physics, Southern University of Science and Technology, No. 1088, Xueyuan Road, Shenzhen, Guangdong, China

<sup>5</sup>Ruder Bošković Institute, Bijenička 54, Zagreb, Croatia

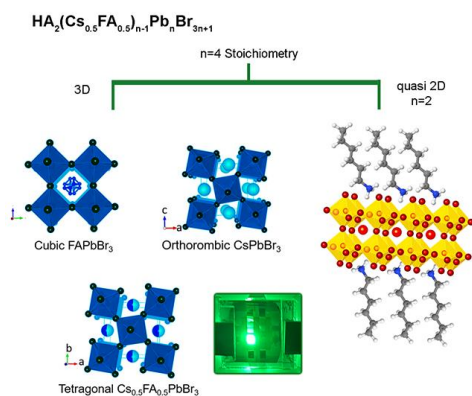
<sup>6</sup>Department of Physics, Faculty of Science, University of Zagreb, Bijenička 32, Zagreb, Croatia

<sup>7</sup>Department of Materials Science and Engineering, City University of Hong Kong, 83 Tat Chee Avenue, Kowloon, Hong Kong

<sup>8</sup>National Synchrotron Radiation Research Center, Hsinchu Science Park, Hsinchu, 30076 Taiwan

<sup>9</sup>Department of Chemical Engineering, National Tsing Hua University, Hsinchu, 30013 Taiwan

### Abstract



The performance of quasi-2D perovskite LEDs with mixed small cations, cesium and formamidinium (FA), is significantly affected by their ratio. The best devices obtained for Cs:FA ratio of 1:1 exhibit a maximum EQE of 12.1%, maximum luminance of 15070  $\text{cd/m}^2$  and maximum current efficiency of 46.1  $\text{cd/A}$ , which is significantly higher (about 3 times) compared to devices with FA only (maximum EQE of 4.1 %, maximum luminance of 4521  $\text{cd/m}^2$ ) and Cs-only (maximum EQE of 4.0%, maximum luminance of 4886  $\text{cd/m}^2$ ). The photoluminescence quantum yield of the Cs:FA 1:1 sample is similarly enhanced, 21.3% compared 5.4% and 6%, for FA-only and Cs-only samples,

respectively. We can observe that the Cs:FA ratio significantly affects the crystallization of the perovskite, with the optimal 1:1 ratio resulting in the formation of tetragonal  $\text{Cs}_{0.5}\text{FA}_{0.5}\text{PbBr}_3$  phase (different from cubic  $\text{FAPbBr}_3$  and orthorhombic  $\text{CsPbBr}_3$ ) with pronounced preferential orientation as well as a significant reduction in the trap density, which leads to a substantial improvement in the light-emitting performance.

## Introduction

Optical properties and light emission from halide perovskites for possible light emitting applications have been intensively studied in recent years.<sup>[1-37]</sup> Among different halide perovskite materials, layered 2D/quasi-2D perovskites have been attracting increasing attention due to their higher exciton binding energies, increased ambient and thermal stability, wider tunability, and the possibility of radiative recombination enhancement by tuning the film composition to achieve efficient energy transfer from higher bandgap to lower bandgap quasi-2D perovskites.<sup>[1]</sup> Different from common 3D halide perovskites with a formula  $ABX_3$ , quasi-2D Ruddlesden-Popper perovskites (RPP) have a general formula  $R_2A_{n-1}B_nX_{3n+1}$ , where  $R^+$  is the bulky amine spacer cation,  $A^+$  is a small organic or alkali metal cation,  $B^{2+}$  is a divalent metal cation,  $X^-$  is a halide anion, and  $n$  is the number of perovskite layers.<sup>[1]</sup> It has been shown that the co-existence of quasi-2D and 3D perovskite results in a significant enhancement of the emission efficiency compared to pure 3D perovskites, as well as improved environmental stability.<sup>[2]</sup> Large organic cations also serve to passivate defects in grain or domain boundaries.<sup>[6]</sup> However, despite these advantages, the achieved efficiencies of quasi-2D perovskite-based LEDs have been limited by non-optimized distributions of different  $n$  phases, and increased defects at surface or grain boundaries.<sup>[7]</sup>

The common approaches to increasing the efficiency of quasi-2D LEDs include optimizing the film composition or deposition to optimize the distribution of quasi-2D phases with different  $n$  to achieve efficient funnelling,<sup>[2,4,5,6,10,12]</sup> using post-treatments to remove excess spacer cations,<sup>[8]</sup> optimizing the device architecture,<sup>[3,9]</sup> or using additives to passivate defects.<sup>[7,15]</sup> The optimization of the film composition would typically involve the optimization of the solution stoichiometry, as well as the choices of spacer cations  $R^+$  and small cations  $B^+$ . Various spacer cations have been reported to date, and common choices involve alkyl chain spacers such as butylammonium (BA), which yielded efficiencies ranging from ~7-16%,<sup>[8,9,12,13,18]</sup> as well as aromatic spacers such as phenethylamine (PEA), which yielded efficiencies in the range ~7-15%.<sup>[3-7]</sup> Among possible small cations  $A^+$ , all three possible choices, namely Cs,<sup>[2,8,9,11]</sup> formamidinium (FA)<sup>[3,6,12]</sup> and methylammonium (MA),<sup>[4,5,18]</sup> have been reported. Recently, the use of mixed cations has been proposed as a feasible method to control the crystallization and consequently film composition and emission efficiency. Both spacer cation<sup>[12]</sup> and small cation<sup>[10,14,19-27]</sup> mixing has been investigated. Small cation mixing approach is particularly interesting since it is applicable to both 3D and quasi-2D perovskite emitters. Different combinations of small cation mixtures have been reported, such as MA-ethylammonium,<sup>[20]</sup> MA-Cs,<sup>[21,25-27]</sup> and Cs-FA,<sup>[10,14,19,22-24]</sup> and the use of mixed cations for both 3D and quasi-2D perovskite based films and devices can result in significant performance improvements compared to the cases with single-cations. However, the reported current efficiencies for 3D perovskite based devices with mixed cations are typically below 15 cd/A,<sup>[23-25]</sup> while higher current efficiencies (~17-54 cd/A) have been reported in quasi-2D perovskite based devices.<sup>[10,19-21]</sup>

In quasi-2D perovskites, the use of mixed small cations was reported to result in improved film quality, changes in the film composition (suppression of phases with small  $n$  number), and reduced efficiency roll-off at higher bias<sup>[10,14,19]</sup> due to suppressed Auger recombination.<sup>[14]</sup> For example, the improvement in performance for CsFA-based quasi-2D perovskite was attributed to improved film quality and lower roughness.<sup>[10]</sup> The incorporation of FA was also found to suppress the formation of undesirable low  $n$  phases.<sup>[10,14]</sup> However,

the effect of small cation mixing on the crystal structure of the mixed phase has not been explored in detail, and how this affect the light emission and LED performance is mostly unknown. Nevertheless, there are indications that the performance enhancement due to the use of mixed small cations has additional effects beyond the suppression of the formation of low  $n$  phases and reduced surface roughness. This is particularly important in Cs-containing devices, where multiple phases of cesium lead bromide are possible, which can lead to complex interplay between sample crystallinity and light emitting performance. For example, it has been reported that the optimized concentration of spacer cation can suppress the formation of unfavourable phase of  $\text{Cs}_4\text{PbBr}_6$  in the quasi-2D perovskite  $\text{PEA}_2(\text{Cs}_{0.5}\text{FA}_{0.5})_{n-1}\text{Pb}_n\text{Br}_{3n+1}$ , resulting in increased light emission for optimized composition.<sup>[19]</sup> In this case, while another possible crystal phase of cesium lead bromide, namely  $\text{CsPb}_2\text{Br}_5$ , has also been detected in  $\text{PEA}_2(\text{Cs}_{0.5}\text{FA}_{0.5})_{n-1}\text{Pb}_n\text{Br}_{3n+1}$ ,<sup>[19]</sup> the detailed implications of its formation on the light emission have not been explored. It has been pointed out that the presence of additional crystal phases such as  $\text{CsPb}_2\text{Br}_5$  and  $\text{Cs}_4\text{PbBr}_6$ , could affect the defect densities and photoluminescence quenching, and these two crystal phases play fundamentally different role in the luminescence of the perovskite emitters. Different synthesis conditions can result in different phases of cesium lead bromide, including  $\text{CsPbBr}_3$ ,  $\text{CsPb}_2\text{Br}_5$ , and  $\text{Cs}_4\text{PbBr}_6$ . These phases can readily transform into each other, and the inclusions of one phase can form within other phases,<sup>[32,37]</sup> and the origin of luminescence of  $\text{CsPb}_2\text{Br}_5$  has been controversial.<sup>[34-36]</sup> Despite these controversies,  $\text{CsPb}_2\text{Br}_5$  phase in particular has been attracting growing attention recently,<sup>[28-37]</sup> and there have been many reports on the efficient  $\text{CsPb}_2\text{Br}_5$ -based<sup>[29]</sup> and  $\text{CsPbBr}_3$ - $\text{CsPb}_2\text{Br}_5$ -based LEDs.<sup>[28,30-32]</sup> It is well known that perovskite materials in general are extremely sensitive to the preparation conditions, leading to different behaviours observed in literature reports. These differences in behaviour are likely to occur due to differences in native defects, which can result in luminescence quenching.<sup>[34]</sup> Nevertheless, the existing reports with enhanced light emission in samples containing  $\text{CsPb}_2\text{Br}_5$  indicates that the improved optical properties can be achieved for optimized samples, and thus it is worth investigating the relationship between the film structure (including the presence of different cesium lead bromide phases), its optical properties, and the device performance.

Here we present a detailed investigation into the crystal structure and optical properties of mixed small cation quasi-2D LEDs. We demonstrate that the ratio of FA and Cs has a significant effect on the structural features of crystalline phases within the thin films, its light emission properties and consequently the device performance. LEDs based on  $\text{Cs}_{0.5}\text{FA}_{0.5}$  emitters clearly outperform devices with both pure Cs and pure FA-based perovskites. The films were prepared using a solution with stoichiometry  $n=4$ , since the films with  $n$  in the range 3-5 typically result in significantly higher PLQY compared to other compositions.<sup>[4,7]</sup> In addition, we have selected hexylammonium (HA) as a spacer cation, since HA-based 2D perovskites exhibit the highest out-of-plane mobility and the lowest self-trapped exciton emission among the alkyl chain spacer cations.<sup>[38]</sup> This is attributed to the fact that both the interlayer distance and spacer cation conformational disorder affect the mobility and broadband emission, resulting in nonlinear dependence on the alkyl chain length.<sup>[38]</sup> While the same behaviour in terms of observed trends in crystal structure and optical properties holds for other spacer cations, such as BA and octylammonium (OA), obtained efficiency of HA-based devices is significantly higher.

## Results and discussion

**Figure 1 a** and **1 b** show the absorption and photoluminescence spectra of  $\text{HA}_2(\text{Cs}_x\text{FA}_{1-x})_{n-1}\text{Pb}_n\text{Br}_{3n+1}$  prepared with  $n=4$  stoichiometry for different Cs content  $x$ . We can observe significant differences in the absorption spectra of the films shown in **Figure 1 a** (vertical lines indicate positions of excitonic peaks corresponding to different  $n$  phases). FA-only films exhibit prominent peaks due to different  $n$  phases for  $n=2, 3, 4$ , etc. which is in agreement with a previous work that reports pronounced absorption peaks corresponding to low  $n$  phases in the case of FA-only samples.<sup>[10]</sup> As the fraction of FA reduces, the absorption peaks corresponding to different  $n$  phases of quasi-2D perovskite are reduced, while the absorption spectrum of the sample corresponding to Cs-only sample does not show evidence of quasi-2D phases. All the films exhibit green emission peak only, and a shift in the emission peak center is observed with increasing FA content (from 513 nm for Cs-only to 534 nm for FA-only), as shown in **Figure 2 c**.

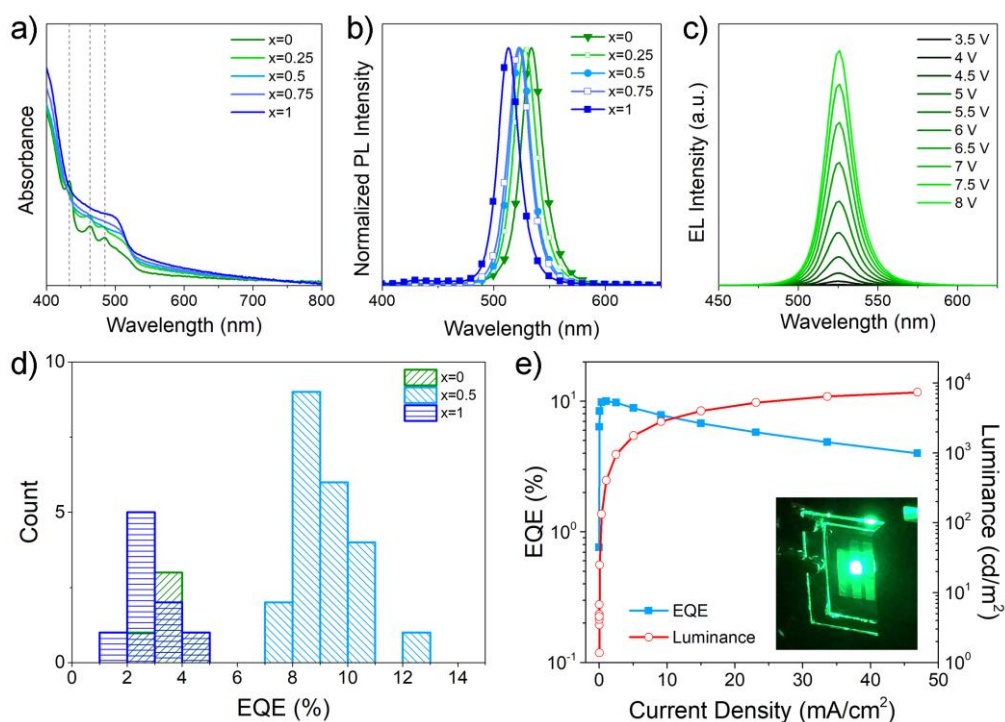


**Figure 1.** a) Absorption and b) normalized PL spectra of  $\text{HA}_2(\text{Cs}_x\text{FA}_{1-x})_{n-1}\text{Pb}_n\text{Br}_{3n+1}$  films with different Cs content  $x$ . c) EL spectra of  $\text{HA}_2(\text{Cs}_{0.5}\text{FA}_{0.5})_{n-1}\text{Pb}_n\text{Br}_{3n+1}$  based LED device as a function of bias voltage. d) EQE histograms of  $\text{HA}_2(\text{Cs}_x\text{FA}_{1-x})_{n-1}\text{Pb}_n\text{Br}_{3n+1}$  based LED devices with  $x=0, 0.5$ , and  $1$ . e) Luminance and EQE of the best  $\text{HA}_2(\text{Cs}_{0.5}\text{FA}_{0.5})_{n-1}\text{Pb}_n\text{Br}_{3n+1}$  based device as a function of current density. Photo of the device is shown in the inset. All the perovskite films were prepared with solution stoichiometry corresponding to  $n=4$ .

However, while films show a consistent and continuous shift in optical properties, a pronounced difference in the performance of LED as function of FA content is observed, with the maximum efficiency significantly enhanced for the Cs:FA ratio of 1:1. The schematic diagrams of the LED and the corresponding energy levels are shown in **Figure S1**, Supporting Information, and the energy levels determined from UPS measurements are also summarized in **Table S1**. EL spectra of the device with  $\text{HA}_2(\text{Cs}_{0.5}\text{FA}_{0.5})_{n-1}\text{Pb}_n\text{Br}_{3n+1}$  active layer for

different bias voltages are shown in **Figure 1 c** while the EL spectra of the devices for additional Cs:FA ratios are shown in **Figure S2**, Supporting Information. Similar to the PL spectra, the emission maximum exhibits red shift with increasing FA content. We can also observe shoulders corresponding to lower  $n$  phase emissions for pure FA devices, which likely contributes to their lower efficiency due to inefficient energy transfer. The performance of the devices for different Cs content  $x$  is summarized in **Table S2**. EQE histograms for devices consisting of  $\text{HA}_2(\text{Cs}_x\text{FA}_{1-x})_3\text{Pb}_4\text{Br}_{13}$  with  $x=0, 0.5$  and  $1$  are shown in **Figure 1 d** while the EQE histograms for additional compositions  $x=0.25$  and  $0.75$  are given in **Figure S3**, Supporting Information. Dramatic enhancement in the performance of  $\text{HA}_2(\text{Cs}_{0.5}\text{FA}_{0.5})_{n-1}\text{Pb}_n\text{Br}_{3n+1}$  devices is observed compared to those with other Cs:FA ratios. The obtained maximum EQE of 12.1%, maximum current efficiency of 46.1 cd/A, and maximum luminance of 15070 cd/m<sup>2</sup> compare favourably to the literature reports on the performance of quasi-2D perovskite-based green LEDs (summarized in **Table S3**, Supporting Information), since our devices, in a large majority of cases, outperform those reported in the literature in at least one of the three performance parameters (EQE, current efficiency, or maximum luminance). It was previously reported that devices exhibited reduced efficiency roll-off when mixed small cations are used,<sup>[10,14,19]</sup> and the use of mixed cations was also reported to result in longer device lifetimes compared to Cs-only devices<sup>[14]</sup> and FA only devices.<sup>[19]</sup> However, here we do not observe significant differences in the EQE dependence on current bias for devices with mixed small cations (**Figure 1 e**) and single small cation devices (**Figure S4**, Supporting Information). The lifetime of the devices with optimal composition is shown in **Figure S5**, for two different initial bias values. The  $T_{50}$  corresponding to initial luminance of 100 cd/m<sup>2</sup> is 32 mins, while longer lifetime of 1.83 h is obtained at lower bias.

Understanding the reasons behind such a significant increase in efficiency and maximum luminance (2-3 times) for  $\text{HA}_2(\text{Cs}_{0.5}\text{FA}_{0.5})_{n-1}\text{Pb}_n\text{Br}_{3n+1}$ , compared to other compositions with different Cs and FA contents, is particularly important in order to identify the crucial factors that have led to remarkable improvement of device performance. Therefore, we performed comprehensive investigations of the film structure and optical properties, in comparison with the perovskites prepared with Cs only and FA only. For the sake of consistency all optical and structural measurements have been performed on the films prepared on TFB polymer, or complete devices in the case of TEM investigations, since the film morphology and the absorption considerably depend on the type of substrates, as shown in **Figure S6**, Supporting Information.

From the TEM images of the devices (**Figures 2 a and b**) we can observe that the mixed films consist of small crystals in a disordered matrix. It has been previously reported that *in situ* formation of nanocrystals can improve light emission from halide perovskite films, which was attributed to a reduction in nonradiative recombination due to nanocrystal surface passivation,<sup>[15,16,18]</sup> and that amorphous lead bromide ammonium complexes located at the surface can be responsible for the luminescence of  $\text{CsPb}_2\text{Br}_5$ .<sup>[36]</sup> No such formation of nanocrystals was observed in single small cation films, as shown in **Figure S7**, Supporting Information. Furthermore, from the HRTEM images shown in **Figure 2**, we can identify the presence of a 3D phase (001 at  $d=5.88$  Å) and a quasi-2D  $n=2$  phase (012 at  $d=7.3$  Å), and we also observe the presence of 3D phase in single cation samples (**Figure S7**, Supporting Information).

The presence of 3D phase and quasi-2D  $n=2$  phase, evident from the absorption spectra and HRTEM, is additionally confirmed by the XRD data. Despite the fact that thin films have been prepared from solutions corresponding to  $n=4$  stoichiometry, XRD analysis revealed dominant presence of 3D perovskite structure ( $\text{APbBr}_3$ ) in all samples, regardless of the choice and ratio of A cation(s). **Figures 2 c- 2 e** show XRD patterns of perovskites obtained by using HA as the spacer cation, while FA,  $\text{Cs}_{0.5}\text{FA}_{0.5}$  and Cs as A-site cations, respectively. XRD patterns for the samples having other compositions at A site including  $\text{Cs}_{0.25}\text{FA}_{0.75}$  and  $\text{Cs}_{0.75}\text{FA}_{0.25}$ , are shown in **Figure S8**, Supporting Information.

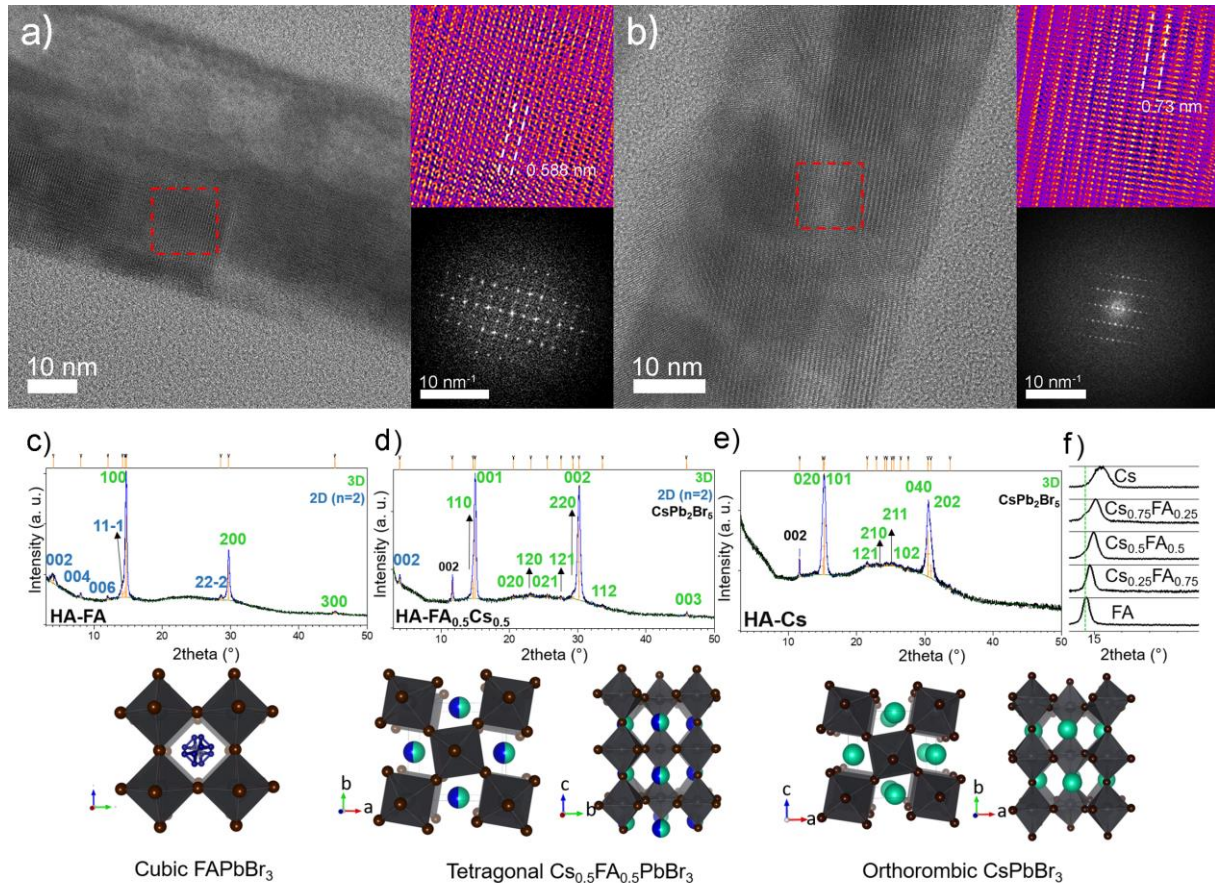


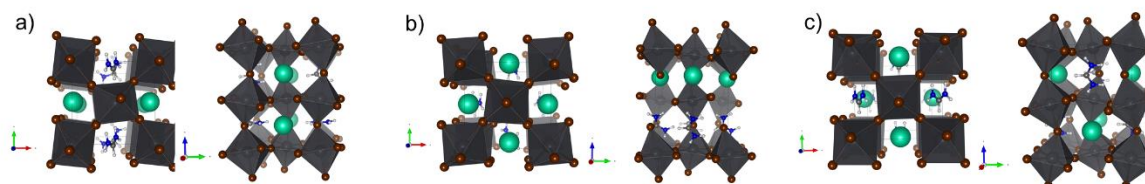
**Figure 2.** a), b) TEM and HRTEM images of  $\text{HA}_2(\text{Cs}_{0.5}\text{FA}_{0.5})_{n-1}\text{Pb}_n\text{Br}_{3n+1}$  films prepared with  $n=4$  stoichiometry, showing 3D and  $n=2$  domains. c-f) XRD patterns of  $\text{HA}_2(\text{Cs}_x\text{FA}_{1-x})_{n-1}\text{Pb}_n\text{Br}_{3n+1}$  films for  $x=0, 0.5$  and 1. Miller indices of 3D reflections ( $\text{APbBr}_3$ ) are given in green while those belonging to  $\text{HA}_2(\text{A})\text{Pb}_2\text{Br}_7$  and  $\text{CsPb}_2\text{Br}_5$  are given in blue and black, respectively.

In the case when A-site is occupied exclusively by FA cations (**Figure 2 c**), the 3D phase exhibits only  $h00$  reflections and it was indexed assuming cubic symmetry with a unit cell parameter  $a = 5.991(2)$  Å, in accordance with literature data.<sup>[39]</sup> Additional Bragg reflections belonging to 3D phase appeared with decreasing amount of FA cations on A site indicating on the tetragonal distortion with the increase in Cs content (**Figure 2 d**). In the case of  $\text{Cs}_{0.5}\text{FA}_{0.5}\text{PbBr}_3$ , the decrease in symmetry becomes evident from the appearance of 110 and 220 reflections at left-hand side of major  $00l$  reflections, at 14.66 and 29.67 ° respectively, as well as from low intensity lines that can be seen from the enlarged region 20-30° in the XRD pattern (**Figure S9**, Supporting Information). We can observe that, in addition

to the reflections at  $\sim 20.5^\circ$  (which can be indexed as tetragonal 020 or cubic 011) and at  $\sim 25.5^\circ$  (which could be indexed as tetragonal 021 or cubic 111), there are additional reflections at  $\sim 22.9^\circ$  and  $27.5^\circ$  which correspond to tetragonal 120 and 121 reflections, respectively, and which could not appear in a cubic cell. The structure of  $\text{Cs}_{0.5}\text{FA}_{0.5}\text{PbBr}_3$  has been refined in the tetragonal  $P4/mbm$  space group with the unit-cell parameters  $a = b = 8.642(2) \text{ \AA}$  and  $c = 5.922(3) \text{ \AA}$ . Refined lattice parameters are smaller compared to the reported similar iodine-based structure,<sup>[40]</sup> due to a smaller ionic radius of bromide.

Although experimental XRD patterns exhibit several features that clearly indicate the symmetry lowering in the case of  $\text{Cs}_{0.5}\text{FA}_{0.5}\text{PbBr}_3$ , density functional theory (DFT) calculations were exploited to gain further insight into the stability of several possible structures, assuming both tetragonal and cubic lattices. As shown in **Figure 3**, seven possible arrangements of A-cations (four within cubic and three within tetragonal lattice) have been studied.

Tetragonal  $\text{Cs}_{0.5}\text{FA}_{0.5}\text{PbBr}_3$



Cubic  $\text{Cs}_{0.5}\text{FA}_{0.5}\text{PbBr}_3$

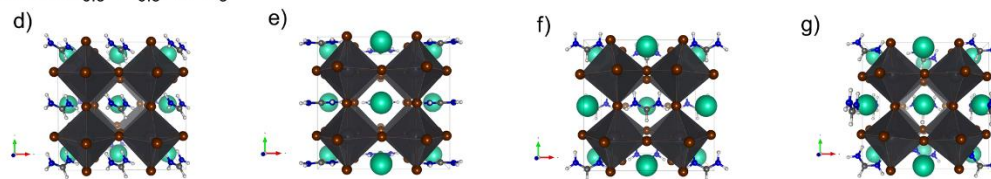


**Figure 3.** Possible arrangements of A cations in tetragonal and cubic  $\text{Cs}_{0.5}\text{FA}_{0.5}\text{PbBr}_3$

Indeed, DFT calculations show that tetragonal lattices of  $\text{Cs}_{0.5}\text{FA}_{0.5}\text{PbBr}_3$  are slightly more stable compared to the cubic structures. Also, it was realized that the structure containing stacks of the same type of cations along  $c$ -direction is more stable compared to the arrangements having layers of the same type cation in  $ab$  plane or those having Cs and FA in alternating *zig-zag* layers in  $ab$  plane. However, the relative energy difference between different assemblies (layered, alternated *zig-zag*, aligned) all lies within 1.2 kcal/mol which is less than  $2kT$ , suggesting that all of the arrangements might easily form in the real samples.

In the case when A-site is occupied by Cs cations exclusively, a further symmetry lowering can be noted from XRD patterns (**Figure 2 e**); it is primarily manifested as a diffraction profile broadening and by the appearance of additional broad low intensity reflections, therefore a full pattern decomposition fitting was performed assuming the orthorhombic symmetry. The structure of  $\text{CsPbBr}_3$  crystallizes in  $Pnma$  space group, adopting a distorted perovskite structure with octahedra tilted with respect to the orthogonal geometry of the ideal perovskite lattice, with the refined unit-cell parameters  $a = 8.248(1) \text{ \AA}$ ,  $b = 11.726(2) \text{ \AA}$ ,  $c = 8.161(2) \text{ \AA}$  which is in an accordance with a structure determined by Kanatzidis *et al.*<sup>[41]</sup> While the diffraction lines  $\sim 23^\circ$  ( $d \sim 3.86$ ) and  $\sim 25.5^\circ$  ( $d \sim 3.49$ ), indexed in orthorhombic cell as 210 and 211, could have also be indexed in higher tetragonal symmetry as 120 and 021, respectively, the rest of the reflections in the range from  $24.4 - 26.5^\circ$  (such as

201, 031, 022) cannot be present in the cubic nor tetragonal symmetry thus their appearance in XRD pattern exclusively confirm the orthorhombic symmetry. **Figure 2 f** shows that the diffraction line positions are shifted to higher  $2\theta$  positions as the Cs molar proportion in the  $\text{FA}_{1-x}\text{Cs}_x\text{PbBr}_3$  films increased due to the difference in radius sizes of A-site cations ( $r(\text{Cs}^+) = 1.81 \text{ \AA}$ ,  $r(\text{FA}^+) = 2.79 \text{ \AA}$ ). The gradual shift of diffraction line positions also confirms the presence of solid solution without phase segregation in the whole range of compositions, in agreement with a previous report.<sup>[14]</sup> We also evaluated formation energy relative to precursor compounds of each 3D perovskite and found that it is the highest for  $\text{FAPbBr}_3$ , while mixed  $\text{Cs}_{0.5}\text{FA}_{0.5}\text{PbBr}_3$  is more favorable by 3.4 kcal/mol and pure  $\text{CsPbBr}_3$  by 10.9 kcal/mol. Besides these internal energies evaluated by DFT, it should be noted that mixing cations additionally gives rise to entropic contribution to stabilization.<sup>[42]</sup>

XRD analysis also shows that the dominant presence of 3D perovskite phase is accompanied by some amount of 2D perovskite ( $n=2$ ) phase and layered  $\text{CsPb}_2\text{Br}_5$  phase (except in the cases of FA-based samples).  $\text{CsPb}_2\text{Br}_5$  phase has been identified based on structure as reported by Huang *et al.*<sup>[43]</sup> The reflections belonging to  $\text{HA}_2\text{FAPb}_2\text{Br}_7$  ( $n=2$ ) structure have been indexed according to similar iodine-based compound  $\text{HA}_2\text{MAPb}_2\text{I}_7$ .<sup>[44]</sup> As expected the crystal lattice of  $\text{HA}_2\text{FAPb}_2\text{Br}_7$  exhibits a smaller periodicity along  $c$ -direction (002 at  $d = 22.02 \text{ \AA}$ ) compared to  $\text{HA}_2\text{MAPb}_2\text{I}_7$  (002 at  $d = 22.37 \text{ \AA}$ ) due to the fact that  $\text{Br}^-$  radius is smaller than  $\text{I}^-$  (even though FA is slightly smaller compared to MA). Similar to 3D phase, diffraction lines belonging to RP  $n=2$  phase exhibit gradual shift of  $00l$  reflections as a function of Cs:FA ratio; 002 line of  $\text{HA}_2\text{FAPb}_2\text{Br}_7$  shifts from  $22.02 \text{ \AA}$  to  $21.56 \text{ \AA}$  for  $\text{HA}_2\text{Cs}_{0.5}\text{FA}_{0.5}\text{Pb}_2\text{Br}_7$  due to the partial incorporation of  $\text{Cs}^+$  instead of  $\text{FA}^+$ . The fact that thin films, although being prepared from solutions corresponding to  $n=4$  stoichiometry, contain mixture of 3D phase and some amount of low-dimensional phase, has additionally being addressed by DFT. The DFT calculations show, although the energy difference is quite small, that the mixture of 3D perovskite and  $n=2$  phase has 0.5 kcal/mol lower energy compared to the pure  $n=4$  phase.

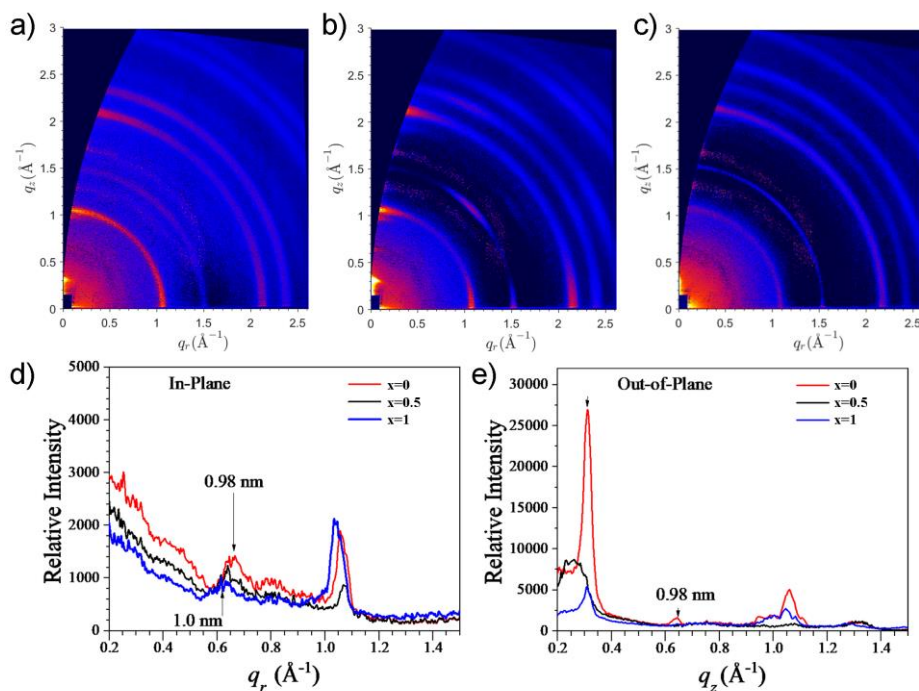


**Figure 4.** GIWAXS 2D patterns for  $\text{HA}_2(\text{Cs}_x\text{FA}_{1-x})_{n-1}\text{Pb}_n\text{Br}_{3n+1}$  films for: a)  $x=0$ , b)  $x=0.5$  and c)  $x=1$  d and e) integrated *in-plane* and *out-of-plane* 1D profiles for  $\text{HA}_2(\text{Cs}_x\text{FA}_{1-x})_{n-1}\text{Pb}_n\text{Br}_{3n+1}$  films for different Cs:FA ratio. Note the highly oriented layering peak along the film-normal direction ( $z$ ) of the CsFA mixing case. All the perovskite films were prepared with solution stoichiometry corresponding to  $n=4$ .

The GIWAXS results shown in **Figure 4** are in excellent agreement with the phases found in the XRD patterns. In addition, the GIWAXS scattering arcs, rather than X-ray diffraction powder ring, observed for the mixed sample indicate highly oriented perovskite crystals along the *out-of-plane* direction of the film, as shown in **Figure 4 e**. Moreover, the GIWAXS data reveal an additional highly oriented peak centered at  $q_z = 0.29 \text{ \AA}^{-1}$  (**Figure 4e**), revealing a layer structure of 2D perovskite of a  $d$ -spacing of 2.16 nm oriented along the film normal direction. Such a layering direction is parallel to the [110] planes of the 3D perovskite crystal structure observed both in GIWAXS and consistently in the XRD. These results suggest that the coexisting 2D and 3D perovskites are particularly orientation-aligned in the mixed sample.

It has been noted that the reflection corresponding to  $d$ -spacing  $\sim 1.0$  nm appears also in the “small spacer cation” type of RP  $n=1$  perovskite structures where small guanidinium (GA) cations, typically present exclusively within the octahedral voids, act as spacer cations.<sup>[45]</sup> Similarly in our case, we might expect the formation of such a special type of RP phase with Cs or FA cations acting as very small spacer cations. Indeed, all-inorganic Ruddlesden-Popper phases  $\text{Cs}_{n+1}\text{Pb}_n\text{Br}_{3n+1}$  have been previously observed in HRTEM,<sup>[46]</sup> while similarly they could not be detected in XRD, but the structure details have not been reported. However, since according to GIWAXS data, this phase is present in all samples, it likely does not contribute to the observed light emitting performance differences and therefore investigation of its formation and properties is beyond the scope of this work.

The transient absorption spectroscopy is commonly used to investigate energy transfer in quasi-2D perovskite films.<sup>[2,5]</sup> From the transient absorption measurements, shown in **Figure 5**, we observe high energy peaks at  $\sim 460$  nm and  $\sim 480$  nm which we attribute as the bleaching of the transitions in the lower  $n$  phases, well aligned with the high energy absorption peak positions in **Figure 1 a**. A large peak at  $\sim 515$  nm, aligned with the absorption band edge, is rapidly populated (the high energy peaks disappear by 10 ps, as shown in **Figure S10**, Supplementary Information) and slowly decays by 1 ns. The TA spectra probed at  $> 200$  ps shows no presence of the high energy peaks likely due to highly efficient energy transfer between different phases (from lower  $n$  towards 3D). Furthermore, this indicates that the presence of quasi-2D perovskites, even at low amounts, still play a significant role in the light emission from the samples. The presence of lower  $n$  phases is also obvious from the extinction coefficient of the samples determined by spectroscopic ellipsometry, shown in **Figure S11**, Supporting information.

Time resolved photoluminescence was performed to investigate the carrier dynamics and recombination of  $\text{HA}_2(\text{Cs}_{1-x}\text{FA}_{0x})_{n-1}\text{Pb}_n\text{Br}_{3n+1}$  thin films for  $x = 0, 0.5$ , and  $1.0$  as shown in **Figure S12**, Supporting Information. Obtained decay curves can be fitted by a bi-exponential function. The decay of  $x = 0$  and  $x = 1$  samples show clearly two distinct components whereas the  $x = 0.5$  sample shows an overall longer decay lifetime. Bi-exponential fittings have been used to characterize perovskite films, where the fast decay component is related to recombination of surface or trap states, and the longer lifetime component is resulted from

radiative decay.<sup>[47,48]</sup> The fast component in  $x=0, 0.5$ , and  $1$ , are  $1.54, 3.68, 1.59$ , with weight fractions of  $0.62, 0.60, 0.64$ , respectively suggesting that the  $x=0$  and  $1$  samples may have increased trap or surface states.

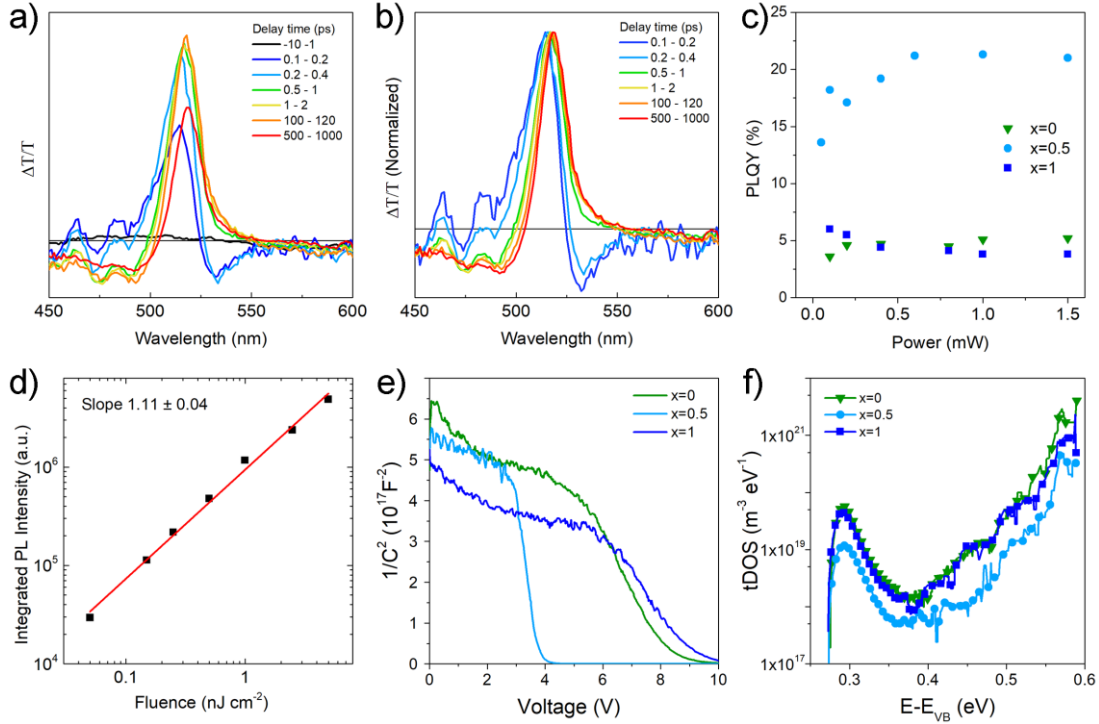


**Figure 5.** a), b) Transient absorption spectra, c) PLQY and d) integrated PL intensity as a function of excitation power of  $\text{HA}_2(\text{Cs}_{0.5}\text{FA}_{0.5})_{n-1}\text{Pb}_n\text{Br}_{3n+1}$  thin film; e) Mott-Schottky plot and f) tDOS of  $\text{HA}_2(\text{Cs}_x\text{FA}_{1-x})_{n-1}\text{Pb}_n\text{Br}_{3n+1}$  based LED devices. All the perovskite films were prepared with solution stoichiometry corresponding to  $n=4$ .

Bi-exponential weighted average lifetimes of  $\tau_{\text{avg}}=9.4$  ns for  $x = 0.5$ ,  $\tau_{\text{avg}} = 4.5$  ns for  $x = 0$ , and  $\tau_{\text{avg}} = 7.4$  ns for  $x = 1$  indicate the higher optical quality of the  $x = 0.5$  film, possibly related to the suppression of non-radiative decay. To gain additional insight into the radiative recombination, we calculate the rates of radiative recombination of the three samples by taking the average lifetimes of the  $x=0, 0.5$  and  $1.0$  and comparing it to the measured PLQY.<sup>[49,50]</sup> Obtained rates are given in **Table S4**, Supplementary Information. The observed reduction in nonradiative recombination rate for  $x=0.5$  sample is in agreement with increased PLQY of  $x = 0.5$  sample, as shown in **Figure 5 c**.

From the obtained PLQY, we can observe significant difference between  $\text{HA}_2(\text{Cs}_{0.5}\text{FA}_{0.5})_{n-1}\text{Pb}_n\text{Br}_{3n+1}$ , exhibiting a maximum PLQY of 21.3%, and  $\text{HA}_2\text{FA}_{n-1}\text{Pb}_n\text{Br}_{3n+1}$  and  $\text{HA}_2\text{Cs}_{n-1}\text{Pb}_n\text{Br}_{3n+1}$  which exhibit maximum PLQY values of 5.4% and 6%, respectively. The decreased lifetime and lower PLQY for samples having Cs content  $x = 1.0$  and  $0$  are attributed to an increase in nonradiative recombination, possibly due to a difference in defect trapping originating from specific structural, but also microstructural, features found for the mixed cation phase compared to those of single cations. It should be noted that the given PLQY values represent external PLQY, and that PLQY measured for thin films on a substrate are limited by the outcoupling and dependent on the sample structure and thus they are not equal internal quantum yield. Knowing the refractive indices and thickness of the layers and external PLQY, we can estimate the escape probability following the previously reported procedure,<sup>[51]</sup> as briefly described in Supporting Information. Thus, for an estimate of internal quantum yield corresponding to externally measured maximum PLQY of 21.3%, we can

obtain values in the range 45-55%, depending on the sample structure for the measurement, as shown in **Table S5**, Supporting Information, which is in good agreement with the LED performance. It should also be noted that these are rough estimates which can be further complicated by the fact that exact sample structure affects not only the outcoupling, but also the layers deposited below or above the perovskite can affect the interfacial trap density, resulting in mismatch between PLQY of films and EQE of the devices. This is illustrated in **Figures S13** and **S14**, Supporting Information, showing the difference in the light emission of perovskite films on different substrates with and without TPBi layer on top of the perovskite. To investigate whether small cation mixing has general positive effect on light emission, we have also prepared nanocrystals in solution (using hexylamine as a ligand). In this case as well we obtained significant PLQY enhancement for  $x=0.5$  samples (PLQY=52.6%), which was much higher than that of FA only (PLQY=31.7%) and Cs-only samples (PLQY=3.6%). The  $x=0.5$  and  $x=1$  samples also clearly showed the presence of tetragonal and orthorhombic structures, respectively, as shown in **Figure S15**, Supporting Information. While the magnitude of enhancement compared to the single cation samples differs for FA and Cs cations, which is expected due to different synthesis procedure for films and nanocrystals, it is obvious that the FA:CS 1:1 ratio still yields significant enhancement of the light emission.

Finally, considering that our samples dominantly contain 3D perovskites, it is necessary to examine the nature of the radiative recombination. It is known that the integrated PL intensity  $I_{PL}$  is described by the power law of the excitation power density  $I_{ex}$ ,  $I_{PL} \sim I_{ex}^k$ , where  $k=2$  corresponds to free carrier recombination,  $1 < k < 2$  corresponds to excitonic recombination, and  $k < 1$  indicates involvement of defects (free-to-bound exciton and donor-acceptor recombination).<sup>[17]</sup> The obtained slope of  $k=1.11 \pm 0.04$  is in good agreement with a previous report on exciton localization in 3D perovskites ( $k=1.179$ ).<sup>[17]</sup> Similar linear dependences are obtained for  $HA_2FA_{n-1}Pb_nBr_{3n+1}$  and  $HA_2Cs_{n-1}Pb_nBr_{3n+1}$ . We note that the PL line shape as well as the peak energy does not change for the different excitation intensities. It should also be noted that defect emissions and/or self-trapped excitons in perovskites are typically associated with broad emissions (FWHM  $\sim 80$  nm) and long PL lifetimes ( $\mu s$  range), while here we observe ns PL lifetimes and narrow emission peaks, which is consistent with the obtained results confirming excitonic recombination. However, it should be noted that these measurements were performed using a femtosecond pulse laser, which results in fast creation of high carrier densities. In the case of PLQY measurement performed using a cw laser diode, we can observe a decrease in PLQY for very low power for  $x=0.5$  samples, which is consistent with trap filling. Nevertheless, for excitation densities for the TRPL measurements, all three samples are in the linear regime corresponding to flat PLQY response in the PLQY power dependence.

Thus, based on the optical and structural investigations, we can conclude that the use of mixed small cations results in a significant alteration of crystallization of the perovskite films, resulting not only in the suppression of the formation of large  $n$  phases observed for pure FA-based samples, but also in the suppression of formation of large crystal domains, observed in pure Cs-based samples. The Cs:FA 1:1 mixed films consist of small crystals in disordered matrix which probably passivate the surface defects and result in improved radiative recombination efficiency. It has been previously proposed that Cs-FA mixed cation perovskite films had fewer traps compared to pure Cs-based perovskite,<sup>[22]</sup> but trap densities were not measured. To examine the defect densities in the films, we have performed

capacitance-voltage measurements, and the resulting Mott-Schottky plot is shown in **Figure 5 e**. The trap density of states (tDOS) of perovskite based LED devices as shown in **Figure 5 f**, was obtained according to the methods reported in the literature.<sup>[53]</sup> Depletion width ( $W$ ) and built-in potential ( $V_{bi}$ ) were calculated from Mott-Schottky measurement at 1 kHz. The Attempt-to-escape frequency  $\omega_0$  was assumed to be  $10^{12} \text{ s}^{-1}$  so that the frequency was converted into energy scale via the following equation:<sup>[53]</sup>

$$E_\omega = k_B T \ln \frac{\omega_0}{\omega}$$

Thus tDOS was calculated by:

$$N_T(E_\omega) = -\frac{V_{bi}}{qW} \frac{dC_p}{d\omega} \frac{\omega}{k_B T}$$

where  $q$ ,  $k_{BT}$ ,  $C_p$  and  $\omega$  are electron charge, thermal energy, capacitance and angular frequency. From the obtained results, we can observe that the built-in potential and the trap density in the mixed small cation films are considerably lower compared to FA- and Cs-based samples. The reduction of the trap density would result in a reduction of non-radiative recombination losses,<sup>[53]</sup> in agreement with the observed enhancement of PLQY and LED performance. Furthermore, we can observe a reduction in the trap density both in deep traps corresponding to surface/interface defects, as well as shallow traps corresponding to defects in the perovskite film (grain boundaries).<sup>[54,55]</sup>

It should also be noted that the observed behaviour applies not only to the perovskites with HA spacer cations, but also to the perovskites with other alkyl chain spacer cations. Absorption and PL spectra of the films with different Cs/FA content with BA and OA spacer cations are shown in **Figures S16** and **S17**, Supporting Information, respectively, while the corresponding GIWAXS patterns and XRD patterns are shown in **Figures S18-S20**, Supporting Information. However, obtained device performances are considerably lower, with the maximum EQE of 0.02% and current efficiency of 0.07 cd/A for BA-based devices, and maximum EQE of 1.73% and current efficiency 6.81 cd/A for OA-based devices. This is likely due to the superior optical and charge transport properties of HA-based perovskites, which represents an optimal length of the alkyl chain spacer taking into account both chain length and its conformational disorder.<sup>[38]</sup>

Thus, this work demonstrates that by controlling the ratio of small cations Cs and FA, we can tailor the crystallization processes occurring in perovskite thin films and thus tune the specific structural and microstructural features of crystalline phases. The optimal ratio of Cs:FA of 1:1 leads to the formation of preferentially grown tetragonal  $\text{Cs}_{0.5}\text{FA}_{0.5}\text{PbBr}_3$  phase that exhibits reduced trap density (compared to FA-only and Cs-only samples) and finally results in significant enhancement of PLQY from 5-6% for single cation samples up to 21.3% for  $\text{Cs}_{0.5}\text{FA}_{0.5}$ -based samples. The LED performance is similarly enhanced, with mixed cation devices exhibiting a maximum EQE of 12.1%, maximum luminance of 15070  $\text{cd/m}^2$  and maximum current efficiency of 46.1 cd/A, which is significantly higher than that of single cation devices which exhibit EQE of ~4% and maximum luminance below 5000  $\text{cd/m}^2$ .

## Experimental Section

### Methods

**Materials.** Lead (II) bromide (98%) and ethanolamine ( $\geq 99\%$ ) were purchased from TCI. Hexthylammonium bromide (HABr), octylammonium bromide (OABr), formamidinium bromide (FABr), and poly[(9,9-dioctylfluorenyl-2,7-diyl)-alt-(4,4'-(N-(4-butylphenyl)) (TFB) are purchased from Xi'an Polymer Light Technology Corporation. n-Butylammonium bromide (BABr) was purchased from Greatcell Solar Materials. Nickel (II) acetate tetrahydrate ( $\text{Ni}(\text{Ac})_2 \cdot 4\text{H}_2\text{O}$ , 99.998%) was purchased from Sigma Aldrich. Chlorobenzene (anhydrous, 99.8%, Sigma Aldrich) and methyl acetate (anhydrous, 99.5%) were purchased from Acros Organics. Cesium bromide (CsBr, 99.999%), 2-propanol (anhydrous, 99.5+%), N,N-dimethylformamide (DMF, anhydrous, 99.9%), and dimethyl sulfoxide (DMSO, anhydrous, 99.9%) were purchased from Alfa Aesar. Hexafluorotetracyano-naphthoquinodimethane (F6TCNNQ, 99%), 1,3,5-Tris(1-phenyl-1H-benzimidazol-2-yl)benzene (TPBi,  $>99.8\%$ ), and 8-hydroxyquinolinolato-lithium (Liq,  $>99.9\%$ ) were purchased from Luminescence Technology Corporation. Aluminum pellets (Al, 99.999%) were purchased from Kurt J. Lesker Company. All materials were directly used as received.

**Synthesis of perovskite thin films.** Precursor solution of various HA based Ruddlesden-Popper perovskites ( $n=4$ ) were prepared by dissolving HABr, CsBr/FABr, and  $\text{PbBr}_2$  with the molar ratio of 2:3:4 in DMSO at a  $\text{Pb}^{2+}$  concentration of 0.4 M.  $\text{NH}_4\text{SCN}$  was dissolved in DMF at a concentration of 0.1 M. The precursor solution was continuously stirred at room temperature overnight. The perovskite precursor solution and  $\text{NH}_4\text{SCN}$  solution were further mixed with volume ratio of 1:1 to obtain a solution at a  $\text{Pb}^{2+}$  concentration of 0.2 M, which was then spin coated on the substrate at 5000 rpm for 35 s. MeAc as the antisolvent was added onto the substrate at 10 s since the start of the spincoating. The as synthesized film was immediately placed in vacuum for 10 min to remove the solvent residues.

**Characterization of perovskite thin films.** Absorption spectra of the perovskite films were obtained using a Cary 50 UV-Vis Spectrometer (Agilent Technologies). Room temperature PL were measured in ambient with a HeCd (325 nm) laser as the excitation source, and the spectra were collected using a PDA-512USB (Control Development Inc.) Fiberoptic Spectrometer. XRD patterns of the perovskite samples were characterized with Rigaku SmartLab 9kW X-ray Diffractometer with Cu  $K\alpha$  radiation. Le Bail refinements have been performed in HighScore Xpert Plus assuming by assuming Split-type pseudo-Voigt profile function and the polynomial background model. During the refinement, a zero shift, scale factor, unit-cell, half-width and peak shape parameters were simultaneously refined. Top view scanning electron microscopy (SEM) was performed using a JEOL JMS-7001F Scanning Electron Microscope. Ultra-violet photoelectron spectroscopy (UPS) characterization of the perovskite samples was performed using an ESCALAB 250 Xi X-ray Photoelectron Spectrometer (Thermal Fisher) with Al  $K\alpha$  radiation (photo energy  $h\nu = 21.2$  eV). To determine the real and imaginary parts of the index of refraction  $n$  and  $k$ , normal incidence transmission (T) and Spectroscopic ellipsometry (SE) measurements at  $50^\circ$ ,  $55^\circ$ ,  $65^\circ$ ,  $70^\circ$  and  $75^\circ$  angle of incidence were collected in the spectral range 0.7 to 6.5 eV using a rotating compensator ellipsometer (J.A. Woollam Inc, model M-2000DI). The SE measurements were performed in two modes: i) covering the backside substrate with a roughened tape yielding the usually measured ellipsometric angles ( $\Psi$ ,  $\Delta$ ); and ii) in reverse direction with the beam incident on the back surface of the glass substrate with corresponding measurements denoted by ( $\Psi_r$ ,  $\Delta_r$ ). The use of a rough-

ened tape is highly efficient to avoid incoherent backside reflections from the substrate that unnecessarily complicate data analysis.<sup>[S1]</sup> The measurements in reverse direction were included to provide additional information and minimize parameter cross-correlation. Data analysis of all data ( $\Psi$ ,  $\Delta$ ,  $\Psi_r$ ,  $\Delta_r$ , and T) was performed using the CompleteEASE software from J.A. Woollam Inc. in the full spectral range assuming the sample is composed of a single bulk film with a surface roughness. We used a parameterized optical model of the dielectric functions consisting of one Tauc-Lorentz oscillator and 8 Gaussian oscillators. Five oscillators at 2.39, 2.47, 2.64, 2.86, and 3.02 eV closely match the resonance energy determined from transient absorption spectroscopy measurements. The remaining three Gaussian oscillators are located in the UV spectral region at 3.29, 4.38, and 6.02 eV.

Time resolved photoluminescence (PL) was measured using a frequency doubled pulsed excitation from a femtosecond Ti:sapphire laser (Coherent Mira 900) operating a 4.2MHz with an output tuned to 400nm. The excitation beam was focused onto the sample and PL was collected by an achromatic lens and diverted into a spectrometer (spectra pro 275) through a 450 nm laser excitation filter. The spectrometer equipped with a 1200 lpmm grating disperses the peak PL wavelength on to a photon counter (Becker and Hickl PMC100) where time correlated single photon counting was performed with a Becker and Hickl SPC photon counting device. Excitation power dependent PL was performed by diverting the PL away from the photon counter with a flip mirror and onto an EMCCD camera (Andor Newton).

Transient absorption was performed using a home built pump probe setup. A Ti:sapphire seed oscillator pumped (Coherent Mira 900) pumps a regenerative amplifier (Coherent Legend Elite), producing a 100 fs pulses at 3.3 mJ of 800 nm at 1 KHz repetition fundamental beam. The fundamental beam is split into two paths, one of the paths enters an optical parametric amplifier (Coherent OPerA Solo) where the pump pulse is generated at 380 nm. This pump beam is diverted onto the sample through a chopper wheel (at 500 Hz), neutral density filters, and a  $\frac{1}{2}$  waveplate to ensure “magic angle” is obtained between the polarization of the pump and the probe. The other split fundamental beam is diverted onto a mechanical delay stage to give time delay between the pump and probe beams. It is then focused onto a 2 mm sapphire plate which generates a broadband supercontinuum (400nm- 1300 nm) acting as the probe beam. The probe beam is passed through a notch filter at 800 nm to cut out the strong fundamental before being focused onto the sample surface with an achromatic lens, spatially overlapping with the pump beam. The transmission of the probe is measured by a spectrometer with a 50lpmm grating and detected with a CCD line array synchronized with the probe laser repetition rate. The transmission spectrum is recorded continuously (1 kHz) and every other shot will be overlapped with the pump beam (500 Hz). Differential signal is then carried out at each time delay point by  $(T_{on}-T_{off})/T_{off}$ . approximately 1000 spectral pairs are taken for averaging for every time point.

The external photoluminescence quantum yield (PLQY) measurements were acquired by exciting the sample with a 405 nm diode laser. The emission signals were detected using a calibrated integrating sphere (Labsphere) together with an Ocean Optics USB2000 spectrometer. The data acquisition and resulting calculation were following a previously reported protocol.<sup>[S2]</sup>

**Density functional theory (DFT) calculations.** For all DFT calculations, a plane-wave basis set code Quantum Espresso was used<sup>[S3,S4]</sup> with the GBRV pseudopotentials<sup>[S5]</sup> and vdW-DF-

cx<sup>[S6]</sup> exchange-correlation functional. The plane-wave basis set cutoff is 816 eV, and the first Brillouin zone is sampled by the Monkhorst–Pack k-point mesh with a density of 5 Å. In each calculation, unit cell and atoms were relaxed until the change in the total energy was <1 meV, forces on each atom were smaller than 0.02 eV Å<sup>-1</sup>, and the pressure was <0.5 kbar.

**Grazing-Incidence Wide-angle X-ray Scattering (GIWAXS).** Perovskite thin films prepared with HA mixed with FA, Cs, or FA-Cs were spin-coated on TFB/quartz substrates (14×14 mm<sup>2</sup>) for GIWAXS. The samples were sealed respectively in a vacuum-tight sample chamber with N<sub>2</sub> flow during GIWAXS data collection, conducted at the BL23A SWAXS instrument of Taiwan Light Source (TLS) of the National Synchrotron Radiation Research Center (NSRRC), Hsinchu.<sup>[S7,S8]</sup> An X-ray beam of 12.0 keV, with an incident angle of 0.2° was used together with a CMOS flat panel detector C10158DK-3957 situated at a sample-to-detector distance of 183.0 mm. With the sample surface defined as the *x*-*y* plane and the incident *x*-rays in the *x*-*z* plane, the scattering vector  $\mathbf{q} = (q_x, q_y, q_z)$  is expressed as  $q_x = 2\pi\lambda^{-1}(\cos\beta\cos\phi - \cos\alpha)$ ,  $q_y = 2\pi\lambda^{-1}(\cos\beta\sin\phi)$ , and  $q_z = 2\pi\lambda^{-1}(\sin\alpha + \sin\beta)$ , with  $\alpha$  and  $\beta$  for the incident and exit angles and  $\phi$  the scattering angle away from the *y*-*z* plane. The in-plane and out-of-plane scattering vector components are respectively defined by  $q_r$  and  $q_z$ , with  $q_r = (q_x^2 + q_y^2)^{1/2}$ , as detailed previously.<sup>[S9,S10]</sup> The scattering peak positions were corrected for the area detector view-angles with respect to the incident beam, and calibrated rigorously with the diffraction peaks from powders of Si, silver-behenate, and LaB<sub>6</sub>.

**High resolution transmission electron microscopy (HRTEM).** Cryo-TEM techniques and cryogenic-STEM techniques were exploited to characterize the morphologies of perovskite samples. The slice samples of the perovskite based LEDs were prepared using an FEI Cryo-FIB Dual Beam focused ion beam/scanning electron microscope system (Helios cryo-SEM/FIB system). A Leica liquid nitrogen cold stage was used for transporting of the samples between the workstation and preparation chamber. Following the cryo-SEM/FIB lift-out preparation procedures, the slice samples were transferred into the cryo-TEM (FEI Krios G3i operated at 300 kV) by liquid nitrogen autoloader. The cryo-TEM system was equipped with a Falcon 3 direct electron detector to obtain TEM images. The operational temperature was maintained at -193.2 °C.

**Fabrication and characterization of perovskite based LED devices.** Patterned ITO/glass substrates were cleaned by sonication in Decon 90, deionized water, acetone, toluene, acetone, and ethanol in sequence, followed by oxygen plasma treatment before use. NiO<sub>x</sub> sol-gel solution was prepared as previously reported,<sup>[S11]</sup> by dissolving 0.2 mmol Ni(Ac)<sub>2</sub>·4H<sub>2</sub>O and 0.2 mmol ethanolamine in 1 mL of 2-propanol. The sol-gel solution was stirred at 70 °C for 2 hours to form a homogeneous green solution. The NiO<sub>x</sub> solution was then spin coated on cleaned ITO/glass substrates at 4000 rpm for 30 s, followed by annealing at 275 °C in air for 30 min. F6TCNNQ as a molecular dopant was dissolved in acetonitrile at a concentration of 0.2 mg/mL. The F6TCNNQ solution was spin coated on the NiO<sub>x</sub> films at 4000 rpm for 30 s inside an Ar-filled glovebox, followed by annealing at 80 °C overnight for effective doping. A TFB thin layer was prepared on top of the doped NiO<sub>x</sub> film by spin coating of TFB solution in chlorobenzene at a concentration of 10 mg/mL, followed by annealing at 120 °C for 30 min.

Perovskite thin films were deposited inside the glovebox following the procedures described above. The as synthesized perovskite films were transferred to the thermal evaporator for thermal deposition of TPBi, Liq, and Al electrodes in sequence with the thicknesses of 40 nm, 2 nm, and 100 nm, respectively. The device area was defined by the cross-sectional area of the ITO and Al electrodes as  $0.04 \text{ cm}^2$ . The device performance of the perovskite LEDs was characterized using a measurement setup consisting of a programmable Keithley 2400 SourceMeter and a Photoresearch PR-670 spectroradiometer with SL-1X close-up lens. The device lifetime was measured by monitoring the luminescence change of the device under a constant current bias.

The frequency-dependent capacitance of the perovskite based devices were measured using a Keysight E4990A Impedance Analyzer in the frequency range of 10 MHz to 20 Hz, 0 V DC, and 25 mV AC amplitude. Depletion width ( $W$ ) and built-in potential ( $V_{bi}$ ) were calculated from Mott-Schottky plots at 1 kHz.<sup>[S12]</sup> The trap density of states (tDOS) was calculated according to the reference.<sup>[S13]</sup>

## Supporting Information

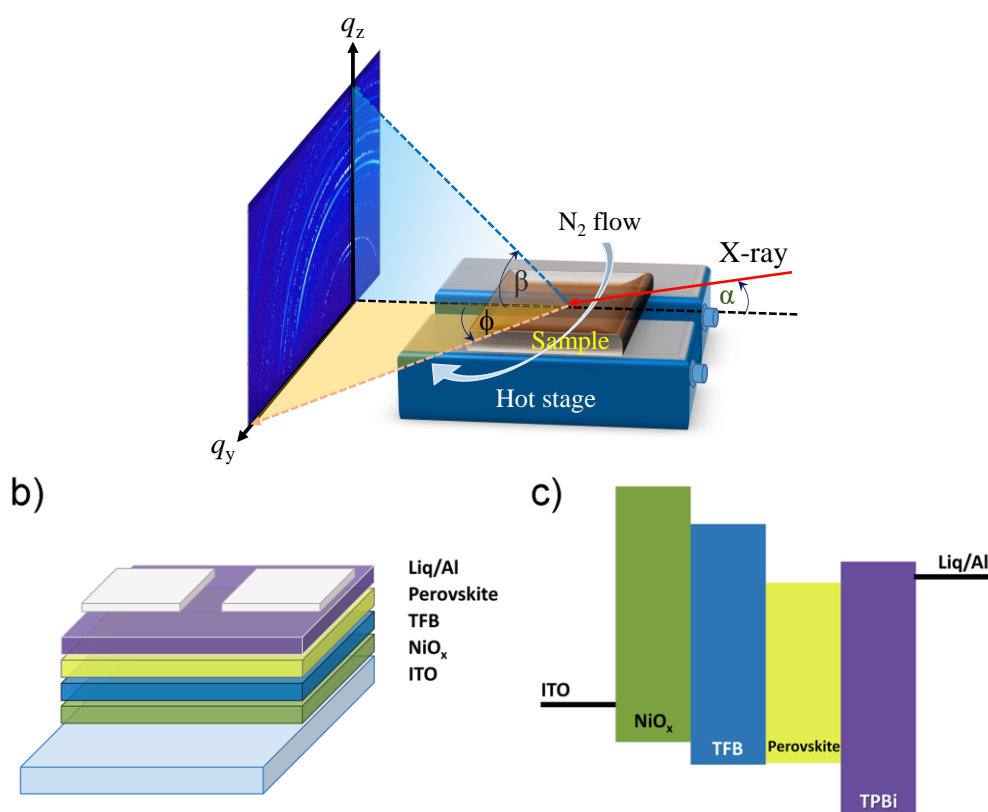


**Figure S1.** a) Schematic view of the GIWAXS setup, with  $N_2$  flow, hot stage, and the beam incident geometry with the incident and scattering angles  $\alpha$ ,  $\beta$ , and  $\phi$ , as reported previously b) Schematic diagram of perovskite LED and c) corresponding energy levels diagram.

**Table S1.** Energy levels and work function of various  $\text{HA}_2(\text{Cs}_x\text{FA}_{1-x})_3\text{Pb}_4\text{Br}_{13}$  films calculated from the UPS spectra.

	$E_{\text{HOMO}}$ (eV)	$\phi$ (eV)
HACs50FA50	5.55	5.2
HACs25FA75	5.58	5.1
HACs75FA25	5.62	5.2
HACs	5.66	5.1
HAFA	5.57	5.2

**Table S2.** Device performance of  $\text{HA}_2(\text{Cs}_x\text{FA}_{1-x})_3\text{Pb}_4\text{Br}_{13}$  based LEDs.

x	Maximum EQE (%)	Maximum Luminance ( $\text{cd}/\text{m}^2$ )	Maximum Current Efficiency ( $\text{cd}/\text{A}$ )	Average EQE (%)	Number of Devices
0	4.08	4521	16.4	$3.58 \pm 0.82$	5
0.25	6.21	11363	24.9	$4.43 \pm 1.19$	7
0.5	12.12	15070	46.1	$9.04 \pm 1.01$	22
0.75	4.99	4886	17.8	$4.21 \pm 0.49$	6
1	4.00	4886	13.0	$2.86 \pm 0.63$	9

**Table S3.** Performance of green-emitting LED devices based on quasi-2D perovskites. The spacer cations/polymer corresponding to the abbreviations in the table are guanidinium (GUA), polyethylene oxide (PEO), 1-naphthylmethylammonium (NMA), phenylbutyl-ammonium (PBA), propylammonium (PA), and benzamidine hydrochloride (BMACl).

Perovskite composition	Maximum EQE (%)	Maximum Luminance ( $\text{cd}/\text{m}^2$ )	Maximum Current Efficiency ( $\text{cd}/\text{A}$ )	Reference
GUA incorporated $\text{CsPbBr}_3$	2.6	>10000	9.4	[S14]
$\text{PEA}_2(\text{FAPbBr}_3)_{n-1}\text{PbBr}_4$	16.4	14240	51.3	[S15]
$\text{PEA}_2(\text{MA})_4\text{Pb}_5\text{Br}_{16}$	7.4	8400	-	[S16]
PEABr doped $\text{FAPbBr}_3$	14.7	37477	-	[S17]
$\text{PEA}_2(\text{FAPbBr}_3)_2\text{PbBr}_4$	14.36	9120	62.4	[S18]
$\text{BA}_2(\text{CsPbBr}_3)_{n-1}\text{PbBr}_4\text{-PEO}$	8.42	33533	25.1	[S19]
$\text{BA}_2\text{Cs}_4\text{Pb}_5\text{Br}_{16}$	16.35	6785	50.0	[S20]
NMABr-CsBr-PbBr <sub>2</sub> -FABr	14.9	$1985.8 \pm 71.6$	46.8	[S21]
$\text{BA}_2\text{Cs}_{n-1}\text{Pb}_n\text{Br}_{3n+1}$	10.1	11200	23.3	[S22]
0.14PABr-0.45PBABr-FAPbBr <sub>3</sub>	15.1	8052	66.1	[S23]
BABr-4PbBr <sub>2</sub> -FABr	7.36	37720	-	[S24]
BABr-5MAPbBr <sub>3</sub>	9.3	2900	17.1	[S25]
$\text{K}_x\text{PEA}_2(\text{FA}_{0.5}\text{Cs}_{0.5})_5\text{Pb}_6\text{Br}_{19}$	5.9	45600	22.5	[S26]
CsBr-PbBr <sub>2</sub> -MABr-BMACl	5.2	12367	17.4	[S27]

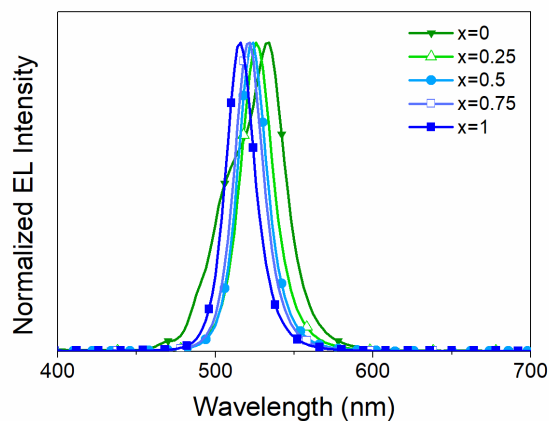


**Figure S2.** Normalized EL spectra of  $\text{HA}_2(\text{Cs}_{0.5}\text{FA}_{0.5})_3\text{Pb}_4\text{Br}_{13}$  based LED devices with  $x=0, 0.25, 0.5, 0.75,$  and  $1$ .

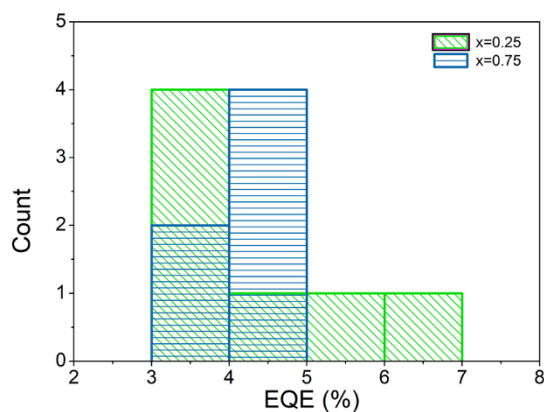


**Figure S3.** EQE histograms of  $\text{HA}_2(\text{Cs}_{0.5}\text{FA}_{0.5})_3\text{Pb}_4\text{Br}_{13}$  based LED devices with  $x=0.25$  and  $0.75$ .

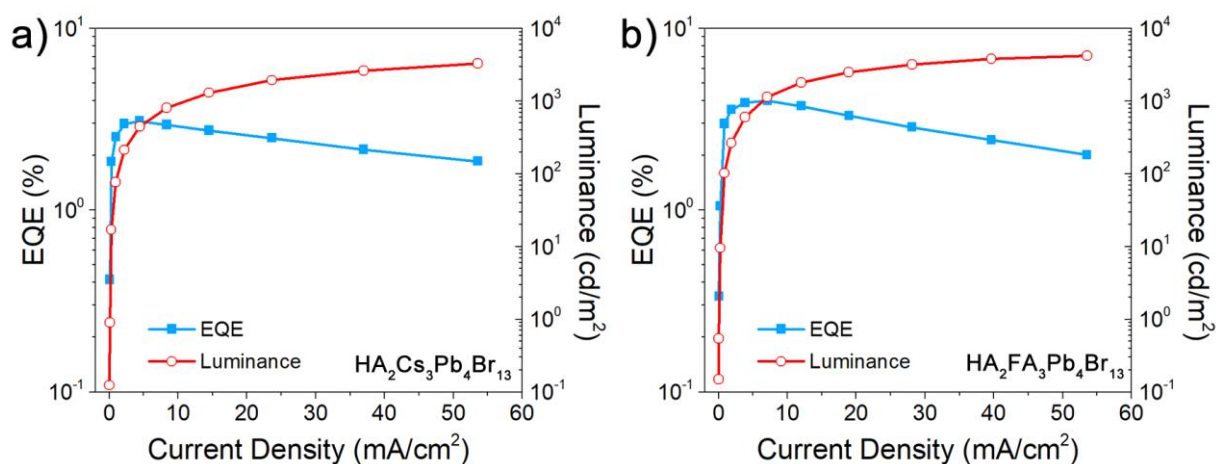


**Figure S4** Luminance and EQE as a function of current density for a)  $\text{HA}_2\text{Cs}_3\text{Pb}_4\text{Br}_{13}$  and b)  $\text{HA}_2\text{FA}_3\text{Pb}_4\text{Br}_{13}$  LEDs.

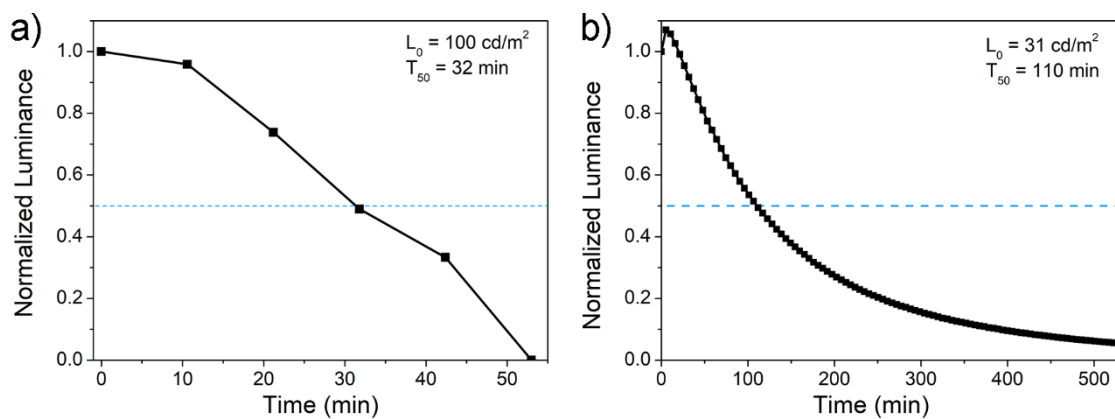


**Figure S5.** Lifetime of  $\text{HA}_2(\text{Cs}_{0.5}\text{FA}_{0.5})_3\text{Pb}_4\text{Br}_{13}$  based LED devices with a) initial luminance of  $100 \text{ cd/m}^2$  b) initial luminance at  $31 \text{ cd/m}^2$ .

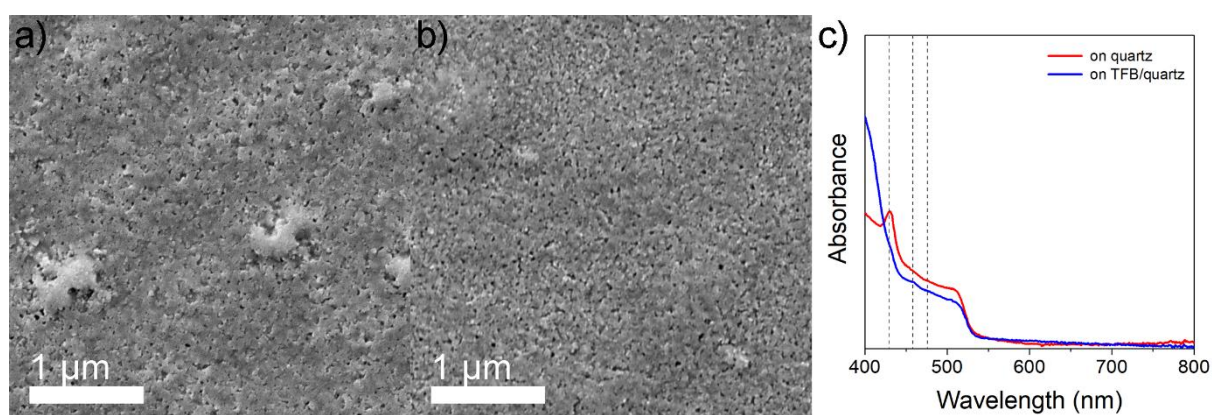


**Figure S6.** a), b) SEM and c) absorption spectra of  $\text{HA}_2(\text{Cs}_{0.5}\text{FA}_{0.5})_3\text{Pb}_4\text{Br}_{13}$  films prepared on ITO/glass and TFB/ITO/glass substrates.

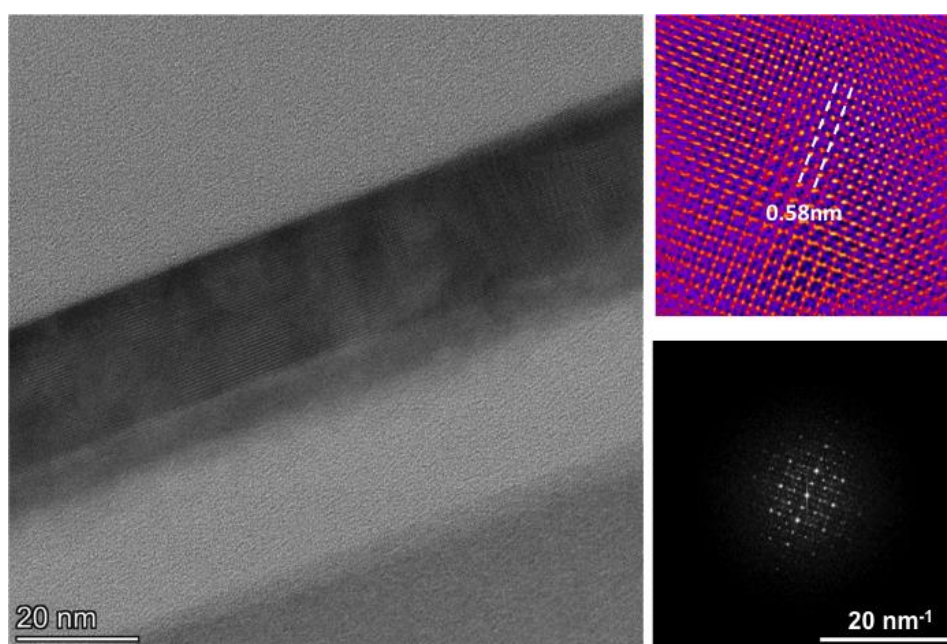


**Figure S7** HRTEM of FA, Cs samples

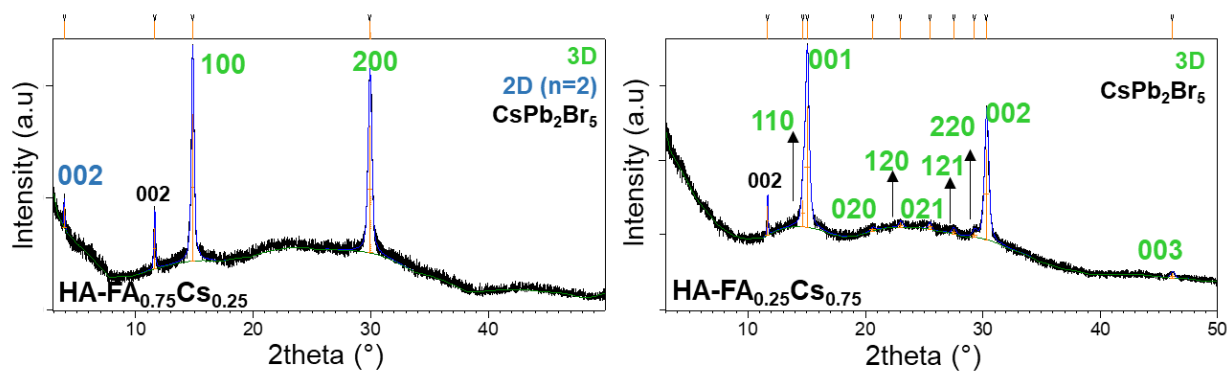


**Figure S8** XRD patterns of mixed cation films  $\text{HA}_2(\text{Cs}_x\text{FA}_{1-x})_3\text{Pb}_4\text{Br}_{13}$  with Cs content  $x$  of 0.25 (left) and 0.75 (right).

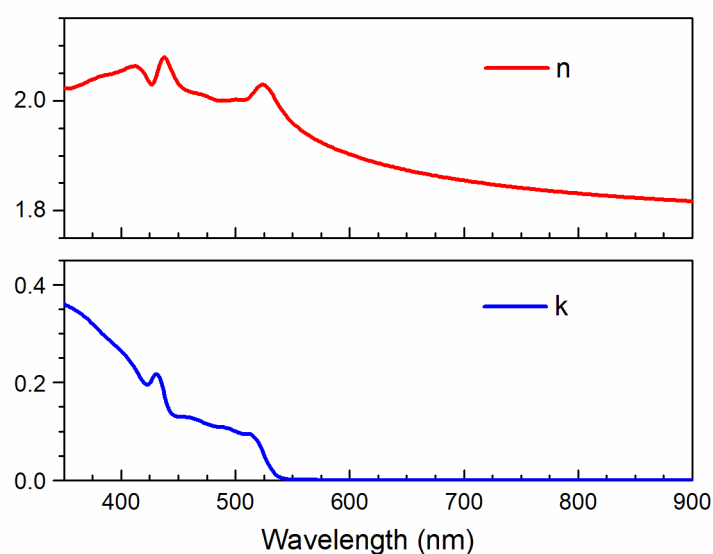


**Figure S9.** The real and imaginary parts of the index of refraction  $\text{HA}_2(\text{Cs}_{0.5}\text{FA}_{0.5})_3\text{Pb}_4\text{Br}_{13}$  thin film determined by spectroscopic ellipsometry.

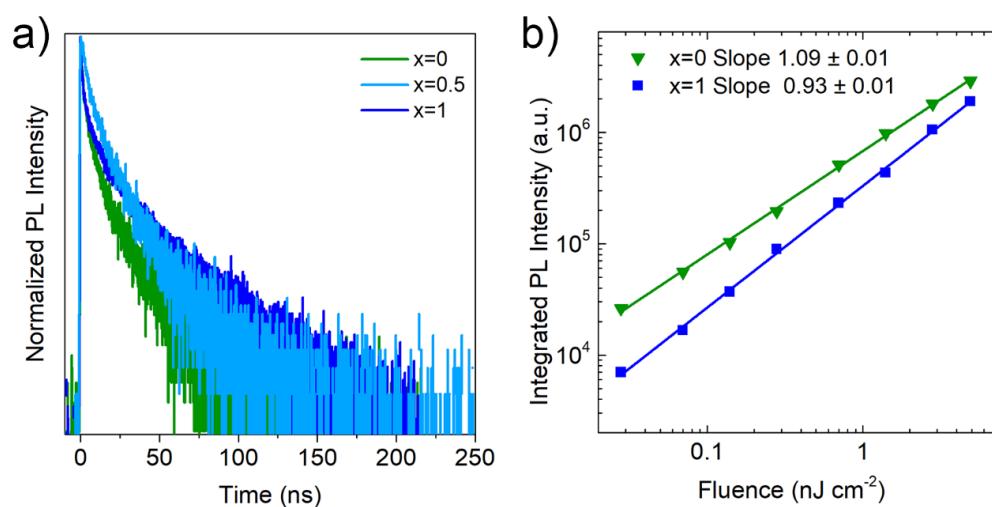


**Figure S10.** a) Time resolved PL spectra of  $\text{HA}_2(\text{Cs}_x\text{FA}_{1-x})_3\text{Pb}_4\text{Br}_{13}$  films with different Cs content  $x$ . b) Integrated PL intensity as a function of excitation power of  $\text{HA}_2(\text{Cs}_x\text{FA}_{1-x})_3\text{Pb}_4\text{Br}_{13}$  films with  $x=0$  and 1.

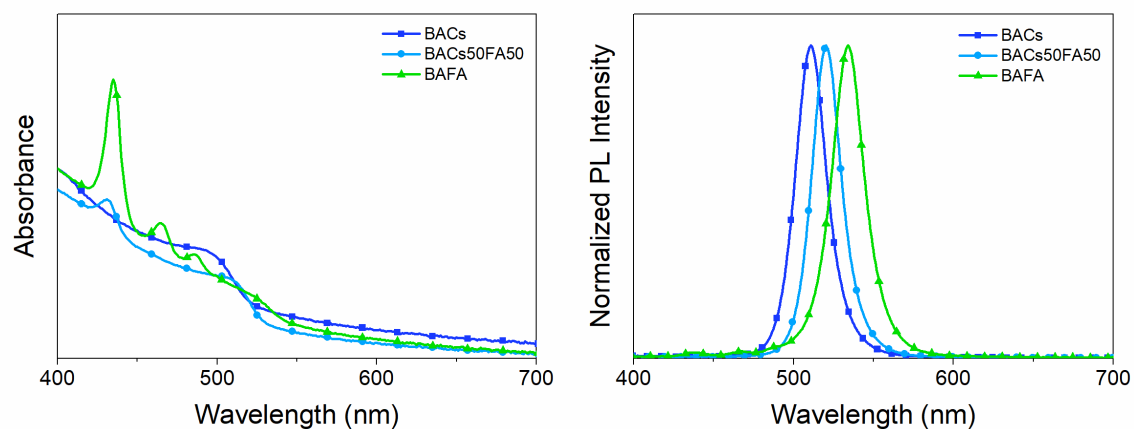


**Figure S11.** a) Absorption and b) normalised PL spectra of  $\text{BA}_2(\text{Cs}_x\text{FA}_{1-x})_3\text{Pb}_4\text{Br}_{13}$  films for different Cs content  $x$ .

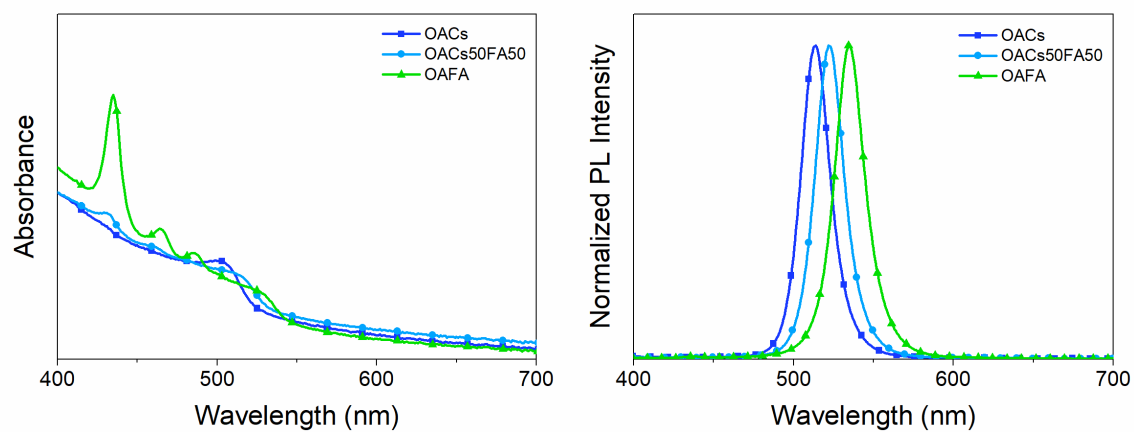


**Figure S12.** a) Absorption and b) normalised PL spectra of  $\text{OA}_2(\text{Cs}_x\text{FA}_{1-x})_3\text{Pb}_4\text{Br}_{13}$  films for different Cs content  $x$ .

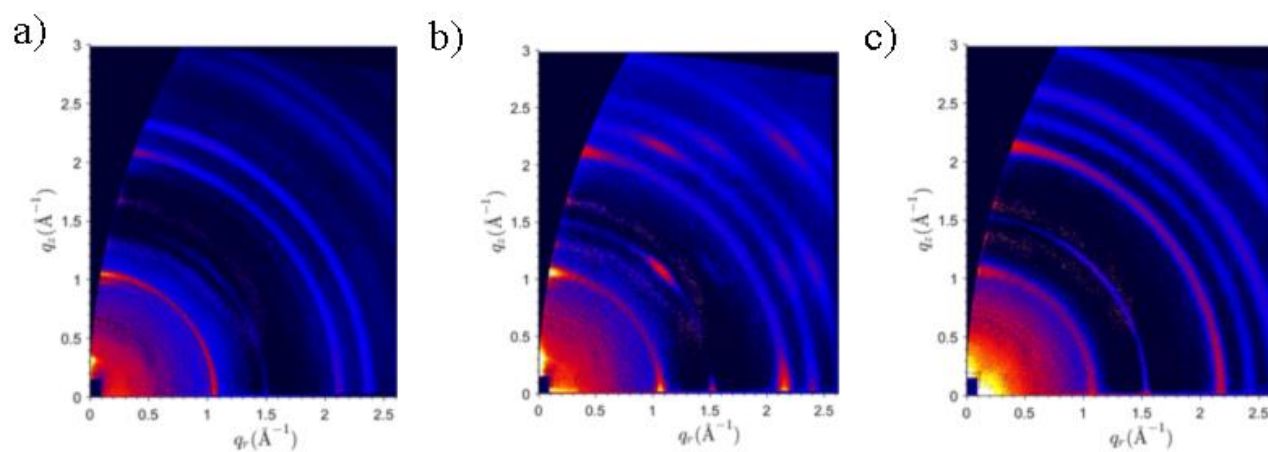


**Figure S13.** GIWAXS 2D patterns for a) BA-FA-, b) BA-(CsFA)-, and c) BA-Cs-based samples.  $x$ .

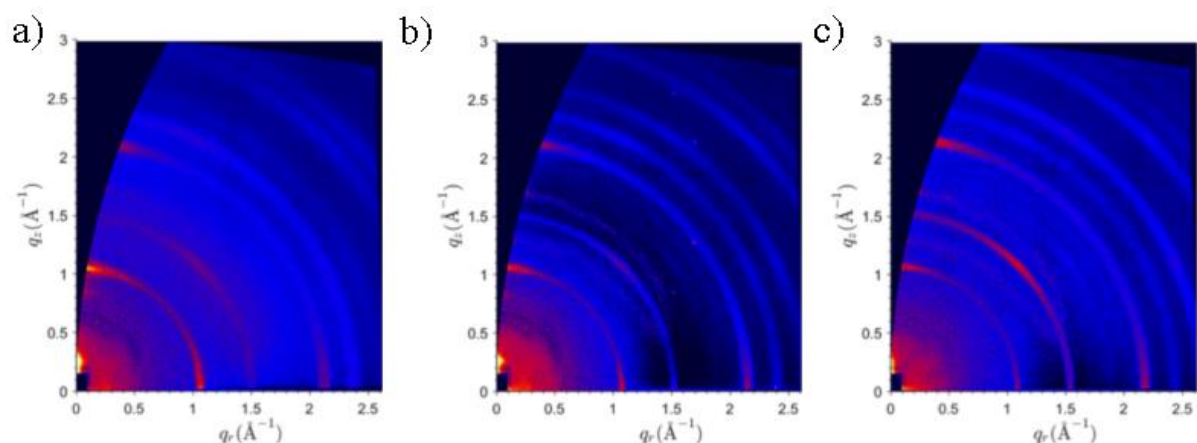


**Figure S14.** GIWAXS 2D patterns for a) OA-FA-, b) OA-(CsFA)-, and c) OA-Cs-based samples.

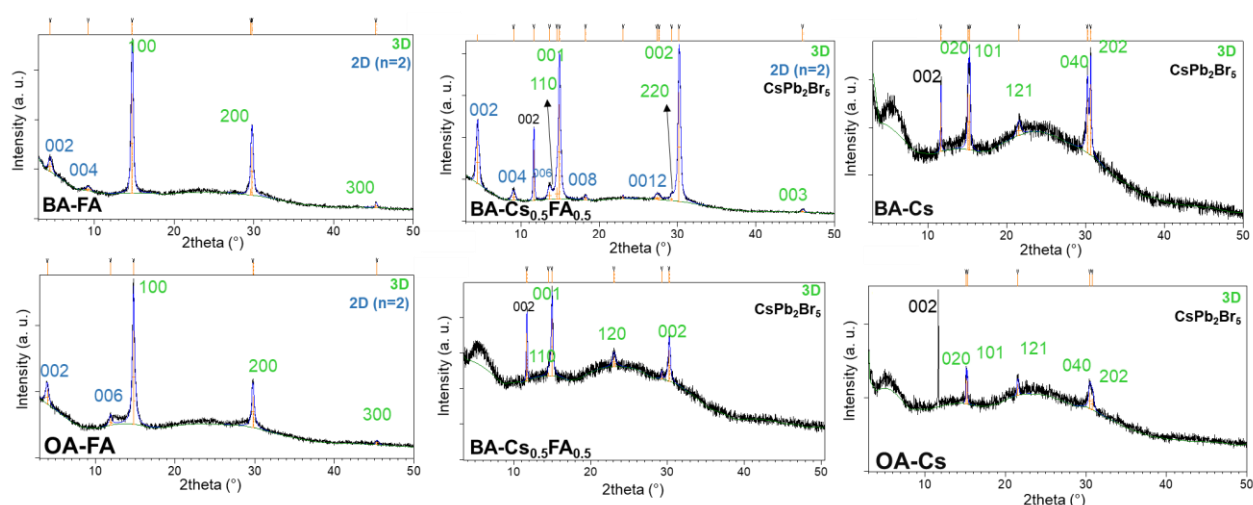


**Figure S15.** XRD of a)  $\text{BA}_2(\text{Cs}_x\text{FA}_{1-x})_3\text{Pb}_4\text{Br}_{13}$  and  $\text{OA}_2(\text{Cs}_x\text{FA}_{1-x})_3\text{Pb}_4\text{Br}_{13}$  films for different Cs content  $x$ .

### Acknowledgements

This work was supported by the Seed Funding for Basic Research and Seed Funding for Strategic Interdisciplinary Research Scheme of the University of Hong Kong, RGC GRF project number 17301520, RGC CRF project 7035-20G, NSFC project 6207032617, PZS-2019-02-2068 project financed by the “Research Cooperability” Program of the Croatian Science Foundation funded by the European Union from the European Social Fund under the Operational Programme Efficient Human Resources 2014-2020, and The Shenzhen Fundamental Research Program (JCYJ20170412154447469). The authors would like to thank Dr. K. H. Low (Chemistry, HKU) for performing XRD measurements.

## References

- [1] F. Zhang, H. Lu, J. Tong, J. J. Berry, M. C. Beard, K. Zhu, *Energy Environ. Sci.* **2020**, 13, 1154.
- [2] W. Cha, H. Han, Y. Hong, G. Kim, C. Park, D. Kim, *J. Phys. Chem. C* **2020**, 124, 4414.
- [3] M. U. Ali, J. Miao, J. Cai, D. F. Perepichka, H. Yang, H. Meng, *ACS Appl. Mater. Interfaces* **2020**, 12, 18761.
- [4] M. Yuan, L. N. Quan, R. Comin, G. Walters, R. Sabatini, O. Voznyy, S. Hoogland, Y. Zhao, E. M. Beauregard, P. Kanjanaboos, Z. Lu, D. H. Kim, E. H. Sargent, *Nat Nanotech.* **2016**, 11, 872.
- [5] L. N. Quan, Y. Zhao, F. P. Garcia de Arquer, R. Sabatini, G. Walters, O. Voznyy, R. Comin, Y. Li, J. Z. Fan, H. Tan, J. Pan, M. Yuan, O. M. Bakr, Z. Lu, D. H. Kim, E. H. Sargent, *Nano Lett.* **2017**, 17, 3701.
- [6] T. Cheng, C. Qin, S. Watanabe, T. Matsushima, C. Adachi, *Adv. Funct. Mater.* **2020**, 30, 2001816.
- [7] X. Yang, X. Zhang, J. Deng, Z. Chu, Q. Jiang, J. Meng, P. Wang, L. Zhang, Z. Yin, J. You, *Nat. Commun.* **2018**, 9, 570.
- [8] Z. Wang, F. Wang, W. Sun, R. Ni, S. Hu, J. Liu, B. Zhang, A. Alsaed, T. Hayat, Z. a. Tan, *Adv. Funct. Mater.* **2018**, 28, 1804187.
- [9] M. You, H. Wang, F. Cao, C. Zhang, T. Zhang, L. Kong, L. Wang, D. Zhao, J. Zhang, X. Yang, *ACS Appl. Mater. Interfaces* **2020**, 12, 43018.
- [10] T. Wu, Y. Yang, Y. Zou, Y. Wang, C. Wu, Y. Han, T. Song, Q. Zhang, X. Gao, B. Sun, *Nanoscale* **2018**, 10, 19322.
- [11] P. Vashishtha, M. Ng, S. B. Shivarudraiah, J. E. Halpert, *Chem. Mater.* **2019**, 31, 83.
- [12] F. Meng, X. Liu, Y. Chen, X. Cai, M. Li, T. Shi, Z. Chen, D. Chen, H. L. Yip, C. Ramanan, P. W. M. Blom, S. J. Su, *Adv. Funct. Mater.* **2020**, 30, 1910167.
- [13] J. Yan, G. Croes, A. Fakharuddin, W. Song, P. Heremans, H. Chen, W. Qiu, *Adv. Opt. Mater.* **2019**, 7, 1900465.
- [14] M. Yang, N. Wang, S. Zhang, W. Zou, Y. He, Y. Wei, M. Xu, J. Wang, W. Huang, *J. Phys. Chem. Lett.* **2018**, 9, 2038.
- [15] F. Liu, C. C. S. Chan, C. Ma, H. W. Tam, T. L. Leung, J. Lin, A. B. Djurišić, K. S. Wong, J. Popović, A. M. C. Ng, W. K. Chan, W. Chen, Z. He, A. E. Adesina, Y. Foo, J. A. Zapien, *Adv. Opt. Mater.* **2019**, 7, 1900269.
- [16] L. Zhao, Y. W. Yeh, N. L. Tran, F. Wu, Z. Xiao, R. A. Kerner, Y. L. Lin, G. D. Scholes, N. Yao, B. P. Rand, *ACS Nano* **2017**, 11, 3957.
- [17] H. He, Q. Yu, H. Li, J. Li, J. Si, Y. Jin, N. Wang, J. Wang, J. He, X. Wang, *Nat. Commun.* **2016**, 7, 10896.
- [18] Z. Xiao, R. A. Kerner, L. Zhao, N. L. Tran, K. Lee, T. W. Koh, G. D. Scholes, B. P. Rand, *Nat. Photonics* **2017**, 11, 108.
- [19] G. Yang, X. Liu, Y. Sun, C. Teng, Y. Wang, S. Zhang and H. Zhou, *Nanoscale* **2020**, 12, 1571.
- [20] Z. Xiao, Q. Wang, X. Wu, Y. Wu, J. Ren, Z. Xiong and X. Yang, *Org. Electron.* **2020**, 77, 105546.
- [21] F. Ye, H. Zhang, P. Wang, W. Li, D. Li, B. Du, D. Liu, T. Wang, *ACS Appl. Mater. Interfaces* **2019**, 11, 43452.

- [22] G. Xie, C. Jiang, J. Wang, C. Mai, G. Huang, Y. Ma, J. Wang, J. Peng, Y. Cao, *Org. Electron.* **2019**, 71, 58.
- [23] H. Cho, J. S. Kim, C. Wolf, Y. H. Kim, H. J. Yun, S. H. Jeong, A. Sadhanala, V. Venugopalan, J. W. Choi, C. L. Lee, R. H. Friend, T. W. Lee, *ACS Nano* **2018**, 12, 2883.
- [24] X. Zhang, H. Liu, W. Wang, J. Zhang, B. Xu, K. L. Karen, Y. Zheng, S. Liu, S. Chen, K. Wang, X. W. Sun, *Adv. Mater.* **2017**, 29, 1606405.
- [25] B. Xu, W. Wang, X. Zhang, W. Cao, D. Wu, S. Liu, H. Dai, S. Chen, K. Wang, X. Sun, *J. Mater. Chem. C* **2017**, 5, 6123.
- [26] J. Si, Y. Liu, N. Wang, M. Xu, J. Li, H. He, J. Wang, Y. Jin, *Nano Res.* **2017**, 10, 1329.
- [27] J. Dai, Y. Fu, L. H. Manger, M. T. Rea, L. Hwang, R. H. Goldsmith, S. Jin, *J. Phys. Chem. Lett.* **2016**, 7, 5036.
- [28] X. Zhang, B. Xu, J. Zhang, Y. Gao, Y. Zheng, K. Wang, X. W. Sun, *Adv. Funct. Mater.* **2016**, 26, 4595.
- [29] C. Qin, T. Matsushima, A. S. D. Sandanayaka, Y. Tsuchiya, C. Adachi, *J. Phys. Chem. Lett.* **2017**, 8, 5415.
- [30] Z. P. Huang, B. Ma, H. Wang, N. Li, R. T. Liu, Z. Q. Zhang, X. D. Zhang, J. H. Zhao, P. Z. Zheng, Q. Wang, H. L. Zhang, *J. Phys. Chem. Lett.* **2020**, 11, 6007.
- [31] B.-S. Zhu, H.-Z. Li, J. Ge, H.-D. Li, Y.-C. Yin, K.-H. Wang, C. Chen, J.-S. Yao, Q. Zhang, H.-B. Yao, *Nanoscale* **2018**, 10, 19262.
- [32] M. Cao, Y. Damji, C. Zhang, L. Wu, Q. Zhong, P. Li, D. Yang, Y. Xu, Q. Zhang, *Small Methods* **2020**, 2000303, 2000303.
- [33] S. K. Balakrishnan, P. V. Kamat, *Chem. Mater.* **2018**, 30, 74.
- [34] S. Caicedo-Dávila, R. Gunder, J. A. Márquez, S. Levchenko, K. Schwarzburg, T. Unold, D. Abou-Ras, *J. Phys. Chem. C* **2020**, 124, 19514.
- [35] T. Zhang, Z. Chen, Y. Shi, Q. H. Xu, *Nanoscale* **2019**, 11, 3186.
- [36] P. Acharyya, P. Pal, P. K. Samanta, A. Sarkar, S. K. Pati, K. Biswas, *Nanoscale* **2019**, 11, 4001.
- [37] Y. B. Cheng, Q. H. Sun, P. Zhang, F. B. Wang, B. B. Zhang, G. D. Zhang, W. Q. Jie, Y. D. Xu, *J. Phys. Chem. Lett.* **2020**, 11, 5625.
- [38] C. Z. Li, J. Yang, F. H. Su, J. J. Tan, Y. Luo, S. J. Ye, *Nature Commun.* **2020**, 11, 5481.
- [39] H. Cho, J. S. Kim, C. Wolf, Y.-H. Kim, H. J. Yun, S.-H. Jeong, A. Sadhanala, V. Venugopalan, J. W. Choi, C.-L. Lee, R. H. Friend, T.-W. Lee, *ACS Nano* **2018**, 12, 2883.
- [40] J. A. Vigil, A. Hazarika, J. M. Luther, M. F. Toney, *ACS Energy Lett.* **2020**, 5, 2475.
- [41] C. C. Stoumpos, C. D. Malliakas, J. A. Peters, Z. Liu, M. Sebastian, J. Im, T. C. Chasapis, A. C. Wibowo, D. Y. Chung, A. J. Freeman, B. W. Wessels, M. G. Kanatzidis, *Cryst. Growth Des.* **2013**, 13, 2722.
- [42] C. Y. Yi, J. S. Luo, S. Meloni, A. Boziki, N. Ashari-Astani, C. Grätzel, S. M. Zakeeruddin, U. Röthlisberger, M. Grätzel, *Energy Environ. Sci.* **2016**, 9, 656.
- [43] Z. Zhang, Y. Zhu, W. Wang, W. Zheng, R. Lin, F. Huang, *J. Mater. Chem. C* **2018**, 6, 446.
- [44] I. Spanopoulos, I. Hadar, W. Ke, Q. Tu, M. Chen, H. Tsai, Y. He, G. Shekhawat, V. P. Dravid, M. R. Wasielewski, A. D. Mohite, C. C. Stoumpos, M. G. Kanatzidis, *J. Am. Chem. Soc.* **2019**, 141, 5518.

- [45] O. Nazarenko, M. R. Kotyrba, S. Yakunin, M. Wörle, B. M. Benin, G. Rainó, F. Krumeich, M. Kepenekian, J. Even, C. Katan, M. V. Kovalenko, *Chem. Mater.* **2019**, 31, 2121.
- [46] Y. Yu, D. D. Zhang, P. D. Yang, *Nano Lett.* **2017**, 17, 5489.
- [47] P. W. Liang, C. Y. Liao, C. C. Chueh, F. Zuo, S. T. Williams, X. K. Xin, J. J. Lin, A. K. Y. Jen, *Adv. Mater.* **2014**, 26, 3748.
- [48] A. H. Slavney, T. Hu, A. M. Lindenberg, H. I. Karunadasa, *J. Am. Chem. Soc.* **2016**, 138, 2138.
- [49] N. Droseros, G. Longo, J. C. Brauer, M. Sessolo, H. J. Bolink, N. Banerji, *ACS Energy Lett.* **2018**, 3, 1458.
- [50] D. K. Sharma, S. Hirata, L. Bujak, V. Biju, T. Kameyama, M. Kishi, T. Torimoto, M. Vacha, *Phys. Chem. Chem. Phys.* **2017**, 19, 3963.
- [51] J. M. Richter, M. Abdi-Jalebi, A. Sadhanala, M. Tabachnyk, J. P. H. Rivett, L. M. Pazos-Outón, K. C. Gödel, M. Price, F. Deschler, R. H. Friend, *Nat. Commun.* **2016**, 7, 13941.
- [52] P. Nandi, C. Giri, D. Topwal, *J. Mater. Chem. C* **2021**, 9, 2793.
- [53] J. Byun, H. Cho, C. Wolf, M. Jang, A. Sadhanala, R. H. Friend, H. Yang, T.-W. Lee, *Adv. Mater.* **2016**, 28, 7515.
- [54] X. Zhang, J. Zhang, D. Phuyal, J. Du, L. Tian, V. A. Öberg, M. B. Johansson, U. B. Cappel, O. Karis, J. Liu, H. Rensmo, G. Boschloo, E. M. J. Johansson, *Adv. Energy Mater.* **2018**, 8, 1702049.
- [55] Z. Ni, C. X. Bao, Y. Liu, W. Q. Wu, S. S. Chen, X. Z. Dai, B. Chen, B. Hartweg, Z. S. Yu, Z. Holman, J. S. Huang, *Science* **2020**, 367, 1352.